

Chiral Symmetry Restoration in the Schwinger Model with Domain Wall Fermions

Pavlos M. Vranas
Columbia University
Physics Department
New York, NY 10027

December 2, 2024

Abstract

Domain Wall Fermions utilize an extra space time dimension to provide a method for restoring the regularization induced chiral symmetry breaking in lattice vector gauge theories even at finite lattice spacing. The breaking is restored at an exponential rate as the size of the extra dimension increases. Before this method can be used in dynamical simulations of lattice QCD, the dependence of the restoration rate to the other parameters of the theory and, in particular, the lattice spacing must be investigated. In this paper such an investigation is carried out in the context of the two flavor lattice Schwinger model.

1 Introduction

When fermions are discretized on a d -dimensional lattice they “double” producing 2^d species for each flavor. In order to remove the unwanted degrees of freedom special care must be taken. For a vector theory, like QCD, two methods have been used to deal with this problem, but both break the global symmetries of the continuum theory. Wilson fermions [1] are implemented by adding an irrelevant operator to the action. This operator makes all but one of the species heavy (with masses close to the cutoff). For the N_f flavor QCD this operator breaks the $SU(N_f)_L \times SU(N_f)_R$ chiral symmetry down to $SU(N_f)$. This explicit breaking is severe and requires fine tuning of the bare quark mass in order to obtain a massless theory. Even then the size of the breaking is proportional to the lattice spacing and only close to the continuum limit the explicit breaking becomes small. Staggered fermions [2] break the $SU(N_f)_L \times SU(N_f)_R$ chiral symmetry down to $U(1) \times U(1)$. Because of the remnant of chiral symmetry the massless theory can be reached by simply taking the bare quark mass to zero. However, the flavor symmetry of the theory has been compromised and is also only recovered as the continuum limit is approached.

Despite these problems both methods have been very successful in describing the light hadron spectrum at zero temperature. However, both methods have difficulties in studying the finite temperature phase transition. Wilson fermions have a complicated phase diagram that, at the presently accessible lattice spacings, makes it hard to extract the relevant physics. Staggered fermions, because of the exact remnant of chiral symmetry, do not suffer from this problem. However, at the presently accessible lattice spacings, the breaking of flavor symmetry makes two of the three pions heavy. This can have important physical consequences since the transition temperature is of the order of the pion mass. For a review on the finite temperature phase transition with both types of fermions the reader is referred to [3] and references therein.

A few years ago a new method for discretizing fermions was developed in order to address the more difficult problems associated with chiral gauge theories [4]. In the following years this method was further developed (see [5] and references therein) with important progress in the development of chiral gauge theories [6], [7]. The basic idea follows from the fact that a massive vector theory in $2n + 1$ dimensions, with a mass term that changes sign along the $2n + 1$ dimension, develops a massless chiral zero mode that is exponentially bound along the $2n + 1$ direction to the region where the mass changes sign. From the point of view of the $2n$ dimensional world this is a chiral fermion. This region is called Domain Wall and this type of fermion is called Domain Wall Fermion (DWF). When such a theory is discretized species doubling also occurs. However, since the $2n + 1$ dimensional theory is vector-like the extra species can be removed with the addition of a standard Wilson term. The resulting theory has a single chiral fermion exponentially bound to the wall. If, for practical reasons, the $2n + 1$ dimension is made finite with periodic boundary conditions for the mass then the mass must change sign one more time. In that region (anti-wall) an exponentially bound chiral zero mode with opposite chirality appears. As a result, the theory becomes vector-like. Different types of boundary conditions yield similar problems. In order to preserve the single chiral mode, the $2n + 1$ dimension must be kept infinite. At first sight this may seem impractical. However, Narayanan and Neuberger developed a method, called the Overlap formalism, that makes it possible to deal with this infinity [6].

The Overlap formalism develops a transfer matrix along the $2n + 1$ dimension and an associated Hamiltonian. The gauge fields are defined only on the $2n$ dimensional space and are taken to be independent of the $2n + 1$ coordinate [6]. In essence, the extra dimension is treated as a complicated flavor space. The resulting formalism involves two Hamiltonians, one for the region of positive mass and one for the region of negative mass. The chiral determinant is the determinant of the overlap of the two ground states associated with each Hamiltonian and it can be calculated explicitly once all the negative eigenvectors of both Hamiltonians are known. For a finite $2n$ dimensional lattice the Hamiltonians are finite size matrices of size $\sim V \times V$ where V is the $2n$ dimensional volume and their eigenvectors can be readily calculated. The resulting chiral determinant has the correct magnitude and a phase that exhibits the correct gauge dependence for “smooth” gauge fields. For “rough” gauge fields the phase exhibits a mild breaking of gauge symmetry even for anomaly free theories. This problem has been resolved in [7].

These methods can also be used to formulate a vector theory. In this case the boundary conditions along the $2n + 1$ dimension are set to be periodic. A Dirac fermion emerges with the positive chirality component bound on the wall and the negative chirality bound on the anti-wall. If the $2n + 1$ dimension is taken to be infinite the two chiralities are decoupled and the resulting theory has intact chiral symmetries! Again, this infinity can be dealt with the Overlap formalism and now there are no issues associated with the phase of the determinant since, for a vector theory, the determinant is real. Therefore, the Overlap formalism provides an ideal lattice regularization of vector theories where the chiral symmetries are left intact even for finite lattice spacing. Also, the anomalous breaking of the axial symmetry is reproduced in an elegant way along with a formula for the index of the chiral Dirac operator [6].

The Overlap formalism was used in a dynamical numerical simulation of the massless single and multiflavor Schwinger model with good results [8]. Numerical simulations of QCD using the overlap formalism would clearly be very appealing. However, as mentioned above, such a simulation would require the calculation of all negative eigenvectors of matrices of size $\sim V \times V$. This makes such a calculation prohibitive for present generation supercomputers.

An obvious alternative (see [5] and references therein) is to keep the $2n + 1$ dimension finite and use standard Hybrid Monte Carlo type algorithms to simulate the theory in $2n + 1$ dimensions. Of course, the exact chiral symmetry will be spoiled but it will be recovered as the size L_s of the $2n + 1$ dimension is sent to infinity. Therefore, even at finite lattice spacing one can control the restoration of the regularization induced chiral symmetry breaking by using the parameter L_s . This involves no fine tuning and, furthermore, since the two chiralities decay exponentially away from the wall (anti-wall), one would expect that the restoration of chiral symmetry would be exponential i.e. $\sim e^{-cL_s}$, $0 < c$. The computer cost of such a simulation would be L_s times larger than a simulation of standard Wilson fermions with the same physical masses. Since for present day supercomputers a value of L_s greater than $10 - 20$ will make simulations impractical, an important question to ask is what is the rate “ c ” of restoration of chiral symmetry and how does it depend on the other parameters of the theory and in particular on the lattice spacing. In [9], [10] some of the issues relating to this question were investigated analytically. Numerical work in [11], [12], [13] has yielded encouraging results and in particular the interesting work

of [13] indicates that DWF can successfully address problems related to the evaluation of weak matrix elements. However, these works have only marginally addressed this particular question. Before full scale dynamical QCD simulations are performed this question should be answered. In this paper this question is investigated in the context of the two flavor lattice Schwinger model.

A useful variation of the wall, anti-wall model studied in [14] was proposed in the context of vector lattice gauge theory in [9], [10]. There, instead of having a mass that changes sign in two places along the $2n + 1$ dimension (say at 0 and $L_s/2$), the mass is kept fixed to some positive value m_0 , but the boundary conditions are taken to be free at the ends of the $2n + 1$ dimension. Again, two zero modes with opposite chiralities emerge, but they are now bound at the opposite ends of the $2n + 1$ dimension and are separated by a distance L_s rather than $L_s/2$ as in the original model. Therefore, the expectation is that for the same L_s this model will achieve better restoration of chiral symmetry.

Another feature added in this model is the introduction of an explicit chiral symmetry breaking term that connects the two ends with strength m_f . This gives mass to the fermion in addition to the one resulting because of the finite extent L_s . The reason for adding this term is that it provides linear control over the fermion mass instead of the exponential one provided by L_s . Furthermore, in a numerical computation, it makes much more sense to vary m_f rather than L_s in order to control the mass. Therefore, for a given m_f one would like to keep L_s large enough so that it does not affect the fermion mass in any significant way. This method and the associated Overlap formalism will be used throughout this paper.

The theory has five parameters. The first two are the lattice spacing a and the physical extent l along one direction of the $2n$ dimensional box (they are controlled by the pure gauge coupling g_0 and the size in lattice units L). The remaining three parameters m_0 , L_s and m_f all control, to some extent, the amount of chiral symmetry breaking and therefore the effective fermion mass. For $L_s \rightarrow \infty$ the theory is chirally symmetric except for the explicit breaking introduced by m_f . As a result, the effective fermion mass vanishes linearly with vanishing m_f [10]. But for finite L_s this is not the case. As mentioned above, even for $m_f = 0$ the restoration of chiral symmetry is expected to be exponential $\sim e^{-cL_s}$.

One would expect that the exact continuum solution of the Schwinger model would be useful to compare with results obtained on the lattice. Unfortunately, this is only partially true. The regularization with DWF introduces to the two dimensional action a four-Fermi term with some coefficient. Since, for the two dimensional model, this operator is not irrelevant, the continuum theory will be different from a continuum theory with no four-Fermi term. Although the continuum theory has been solved with such a term present [15], the results can not be directly compared since the value of the coefficient arising from the DWF has not been calculated. This problem was encountered in [8] and [7] and made the comparison with continuum results complicated. Fortunately, for the purposes of this work, the continuum results are not needed. In fact, there is a much more relevant comparison that can be made. At every step the value of any observable at finite L_s can be directly compared with its value at infinite L_s calculated using the Overlap on the same lattice size and lattice spacing.

The paper is organized as follows: In section 2 the model and the corresponding Overlap implementation is reviewed. In section 3 the definitions of the various observables used

in this paper are given. In section 4 the free theory for finite L_s is discussed, the full expression for the propagator is given and the “effective” bare fermion mass is identified. In section 5 some general considerations regarding the interacting theory are presented. These considerations lead to specific predictions. In section 6 the results of a full dynamical simulation using the Overlap with non zero mass are presented. These results, interesting in their own right, are used to compare with the finite L_s results of the next section. Section 7 describes the results of a dynamical simulation of the $2 + 1$ dimensional system for various values of the parameters on a fixed physical volume. The algorithm used is a standard Hybrid Monte Carlo (HMC) algorithm. The numerical results confirm the predictions made in section 5 and together outline the mechanisms of chiral symmetry restoration in the model. Section 8 contains a summary and conclusions.

2 The Model

In this section the model and the corresponding Overlap formalism [6] implementation is reviewed for the benefit of the reader and in order to establish notation [9], [10]. The following is for a single flavor. The generalization to more flavors is straightforward.

The partition function of the single flavor $2n + 1$ dimensional model is:

$$Z = \int [dU] \int [d\bar{\Psi} d\Psi] \int [d\Phi^\dagger d\Phi] e^{-S} \quad (1)$$

$U_\mu(x)$ is the gauge field, $\Psi(x, s)$ is the fermion field and $\Phi(x, s)$ is a bosonic Pauli Villars (PV) type field. x is a coordinate in the $2n$ dimensional space-time box with extent L along each of the directions, $\mu = 1, 2, \dots, 2n$, and $s = 0, 1, \dots, L_s - 1$, where L_s is the size of the $2n + 1$ direction and is taken to be an even number. The action S is given by:

$$S = S(g_0, L, L_s, m_0, m_f) = S_G(U) + S_F(\bar{\Psi}, \Psi, U) + S_{PV}(\Phi^\dagger, \Phi, U) \quad (2)$$

where:

$$S_G = \frac{1}{g_0^2} \sum_p \text{Re} \text{Tr}[I - U_p] \quad (3)$$

is the standard plaquette action with g_0 the lattice gauge coupling. In this paper the coupling g_0 is exchanged for the parameter:

$$(\mu l) = \frac{g_0}{\sqrt{\pi}} L \quad (4)$$

where l is the physical size of the $2n$ dimensional box along one of its dimensions and μ is a mass related to the photon mass with:

$$m_\gamma = \sqrt{N_f} \mu \quad (5)$$

where N_f is the number of flavors. With these choices μl is the physical box size in units of μ and $\mu l / L = \mu a$ is the lattice spacing in units of μ .

The fermion action is:

$$S_F = \sum_{x, x', s, s'} \bar{\Psi}(x, s) D_F(x, s; x', s') \Psi(x', s') \quad (6)$$

with the fermion matrix given by:

$$D_F(x, s; x', y') = \delta(s - s') \mathcal{D}(x, x') + \mathcal{D}^\perp(s, s') \delta(x - x') \quad (7)$$

$$\begin{aligned} \mathcal{D}(x, x') &= \frac{1}{2} \sum_{\mu} \left[(1 + \gamma_{\mu}) U_{\mu}(x) \delta(x + \hat{\mu} - x') + (1 - \gamma_{\mu}) U_{\mu}^{\dagger}(x') \delta(x' + \hat{\mu} - x) \right] \\ &+ (m_0 - 2n) \delta(x - x') \end{aligned} \quad (8)$$

$$\mathcal{D}^\perp(s, s') = \begin{cases} P_R \delta(1 - s') - m_f P_L \delta(L_s - 1 - s') - \delta(0 - s') & s = 0 \\ P_R \delta(s + 1 - s') + P_L \delta(s - 1 - s') - \delta(s - s') & 0 < s < L_s - 1 \\ -m_f P_R \delta(0 - s') + P_L \delta(L_s - 2 - s') - \delta(L_s - 1 - s') & s = L_s - 1 \end{cases} \quad (9)$$

$$P_{R,L} = \frac{1 \pm \gamma_5}{2} \quad (10)$$

where m_0 is a $2n + 1$ dimensional mass representing the “height” of the Domain Wall. In order for the doubler species to be removed one must set $0 < m_0 < 2$ [4]. However, this range is further restricted by the requirement that the transfer matrix along the $2n + 1$ direction be positive [6]:

$$0 < m_0 < 1 \quad (11)$$

The gamma matrices are taken in the chiral basis and are the same as in the last reference in [6]. In two dimensions they are:

$$\gamma_1 = \begin{pmatrix} 0 & 1 \\ 1 & 0 \end{pmatrix}, \quad \gamma_2 = \begin{pmatrix} 0 & i \\ -i & 0 \end{pmatrix}, \quad \gamma_5 = \begin{pmatrix} 1 & 0 \\ 0 & -1 \end{pmatrix} \quad (12)$$

The PV action is designed to cancel the contribution of the heavy fermions in the large L_s limit. This is necessary because the number of heavy fermions is $\sim L_s$ and at the $L_s \rightarrow \infty$ limit they produce bulk type infinities [6]. There is some flexibility in the definition of the PV action since different actions could have the same $L_s \rightarrow \infty$ limit. However, the choice of the PV action may affect the approach to the $L_s \rightarrow \infty$ limit. A slightly different action than the one used in [10] is used here. This action is easier to implement numerically and for finite L_s it projects the ground state of the transfer matrix T better; the projector is T^{L_s} instead of $T^{L_s/2}$ (see below). Also, even for finite L_s , it exactly cancels out the fermion action when $m_f = 1$ resulting into a pure gauge theory. The PV action is:

$$S_{PV} = \sum_{x, x', s, s'} \Phi^{\dagger}(x, s) D_F[m_f = 1](x, s; x', y') \Phi(x', s') \quad (13)$$

The transfer matrix along the $2n + 1$ direction for this model is:

$$T = e^{-\hat{a}^{\dagger} H \hat{a}} \quad (14)$$

where $\hat{a}^{\dagger}, \hat{a}$ are creation and annihilation operators that obey canonical anticommutation relations and span a Fock space with vacuum state $|0\rangle$. These operators live on the sites of the $2n$ dimensional lattice and carry spin, color and flavor indices. The left/right component decomposition of \hat{a} is:

$$\hat{a} = \begin{pmatrix} \hat{c} \\ \hat{d}^{\dagger} \end{pmatrix} \quad (15)$$

The single particle Hamiltonian H is defined by:

$$e^{-H} = \begin{pmatrix} B^{-1} & B^{-1}C \\ C^\dagger B^{-1} & C^\dagger B^{-1}C + B \end{pmatrix} \quad (16)$$

$$B(x, y) = \frac{1}{2} \sum_{\mu=1}^{2n} \left[2 - U_\mu(x) \delta(x + \hat{\mu} - y) - U_\mu^\dagger(y) \delta(y + \hat{\mu} - x) \right] + (1 - m_0) \delta(x - y) \quad (17)$$

$$C(x, y) = \frac{1}{2} \sum_{\mu} \left[U_\mu(x) \delta(x + \hat{\mu} - y) - U_\mu^\dagger(y) \delta(y + \hat{\mu} - x) \right] \sigma_\mu \quad (18)$$

with $\sigma_1 = 1, \sigma_2 = i$ in two dimensions.

The fermionic and PV effective actions can be expressed in terms of the transfer matrix as:

$$e^{-S_{\text{eff}}^F[L_s]} = \det(D_F[m_f]) = \det(B)^{L_s} \text{Tr} \left[T^{L_s} \mathcal{O}(m_f) \right] \quad (19)$$

$$e^{-S_{\text{eff}}^{PV}[L_s]} = (\det(D_F[m_f = 1]))^{-1} = \left(\det(B)^{L_s} \text{Tr} \left[T^{L_s} \right] \right)^{-1} \quad (20)$$

where the operator $\mathcal{O}(m_f)$ implements the boundary conditions and contains all the m_f dependence:

$$\mathcal{O}(m_f) = \prod_n (\hat{c}_n \hat{c}_n^\dagger + m_f \hat{c}_n^\dagger \hat{c}_n) (\hat{d}_n \hat{d}_n^\dagger + m_f \hat{d}_n^\dagger \hat{d}_n) \quad (21)$$

For $m_f = 1$ it is the identity operator and for $m_f = 0$ is a projection operator to a state $|0'>$:

$$|0> = \prod_n \hat{d}^\dagger |0'> \quad (22)$$

In the infinite L_s limit T^{L_s} becomes a projection operator to the ground state of $-\hat{a}^\dagger H \hat{a}$,

$$\lim_{L_s \rightarrow \infty} T^{L_s} \rightarrow e^{-\lambda_0} |0_H> <0_H| \quad (23)$$

where $|0_H>$ and λ_0 are the ground state eigenvector and eigenvalue of $\hat{a}^\dagger H \hat{a}$ obtained by filling all negative energy states. To get an explicit relation between $|0_H>$ and $|0>$ let R be the eigenvector matrix of the single particle Hamiltonian H . The matrices H and R have size $N \times N$ where $N = \text{spin} \times \text{color} \times \text{flavor} \times V$. R can be put in the form:

$$R = \begin{pmatrix} P^- & P^+ \\ Q^- & Q^+ \end{pmatrix} \quad (24)$$

where the rows labeled P correspond to the left chirality states (with creation/annihilation operators \hat{c}^\dagger, \hat{c}) and the rows labeled Q correspond to the right chirality states (with creation/annihilation operators \hat{d}^\dagger, \hat{d}). The \pm splitting of the columns corresponds to eigenvectors with positive/negative eigenvalues. With N^\pm denoting the number of positive/negative eigenvalues the size of the P^-, Q^- matrices is $N/2 \times N^-$ and the size of the P^+, Q^+ matrices is $N/2 \times N^+$. Then it can be shown that:

$$|0_H> = \prod_{i=1}^{N^-} (\hat{c}_{l_i}^\dagger P_{l_i, i}^- + \hat{d}_{l_i} Q_{l_i, i}^-) |0> \quad (25)$$

From equations 19, 20 and 23 the effective action for the fermion and PV fields in the $L_s -> \infty$ limit is given by the Overlap formula:

$$e^{-S_{\text{eff}}[L_s=\infty, m_f]} = e^{-S_{\text{eff}}^F[L_s=\infty, m_f] - S_{\text{eff}}^{PV}[L_s=\infty]} = \langle 0_H | \mathcal{O}(m_f) | 0_H \rangle \quad (26)$$

For $m_f = 1$, $\langle 0_H | \mathcal{O}(1) | 0_H \rangle = 1$, corresponding to a theory with no fermions. The $m_f = 0$ case corresponds to massless fermions and the Overlap takes the special form:

$$e^{-S_{\text{eff}}[L_s=\infty, m_f=0]} = |\langle 0_H | 0' \rangle|^2 \quad (27)$$

It can be shown that:

$$|\langle 0_H | 0' \rangle|^2 = |\det(Q^-)|^2 \quad (28)$$

If $N^- = N/2$, Q^- is a square matrix and the Overlap will in general be non zero. However, if $N^- \neq N/2$ then Q^- is not a square matrix and its determinant is identically zero. From equations 22, 25 and 28, one can see that this arises because of a mismatch in the filling levels of $|0_H\rangle$ and $|0'\rangle$. In order to obtain a non zero overlap one would need to insert the appropriate number of creation and annihilation operators to balance the filling levels. In fact these operators are the t'Hooft vertices constructed with lattice fields. Then an elegant definition of the topological charge q as seen by the fermions arises, [6]:

$$q = N^- - N/2 \quad (29)$$

where q is naturally integer valued.

When $m_f \neq 0$ use of equations 21, 25 and 26 yield explicit expressions for the Overlap as a determinant of a matrix that is constructed out of P^- and Q^- . These expressions are used in the numerical simulation of the Overlap ($L_s \rightarrow \infty$) in section 6. For more details the reader is referred to [6] and [9], [10].

3 Observables

In this section the definitions of the observables that are measured in this paper are given. The operators involved are as in [6], [10].

The $2n$ dimensional fermion operators of the $2n+1$ dimensional theory are constructed out of the $2n$ dimensional fermion fields $\bar{\psi}, \psi$ as in [10]:

$$\begin{aligned} \psi(x) &= P_R \Psi(x, 0) + P_L \Psi(x, L_s - 1) \\ \bar{\psi}(x) &= \bar{\Psi}(x, L_s - 1) P_R + \bar{\Psi}(x, 0) P_L \end{aligned} \quad (30)$$

In the $L_s \rightarrow \infty$ limit of the theory these operators exactly correspond to insertions in the Overlap of the creation and annihilation operators discussed in section 2. This will allow explicit comparisons to be made between measurements involving $\bar{\psi}, \psi$ in the $2n+1$ theory with finite L_s and measurements with the Overlap involving the corresponding creation and annihilation operators.

The following is a list of definitions of the observables for any L_s and the corresponding Overlap expressions. The definitions of the actions are as in section 2 but for two flavors. Use is made of the fact [10]:

$$\det(D_F) = \det(D_F^\dagger) \quad (31)$$

The fermion effective action of the $2n + 1$ dimensional theory in a background gauge field is:

$$e^{-S_{\text{eff}}^F[L_s, m_f]} = \int [d\bar{\Psi} d\Psi] e^{-S_F} = \det(D_F^\dagger[L_s, m_f] D_F[L_s, m_f]) \quad (32)$$

The PV effective action in a background gauge field is:

$$e^{-S_{\text{eff}}^{PV}[L_s]} = \int [d\bar{\Psi} d\Psi] e^{-S_{PV}} = \det(D_F^\dagger[L_s, m_f = 1] D_F[L_s, m_f = 1])^{-1} \quad (33)$$

The fermion effective action in a background gauge field is:

$$e^{-S_{\text{eff}}[L_s, m_f]} = e^{-S_{\text{eff}}^F[L_s, m_f] - S_{\text{eff}}^{PV}[L_s]} = \frac{\det(D_F^\dagger[L_s, m_f] D_F[L_s, m_f])}{\det(D_F^\dagger[L_s, m_f = 1] D_F[L_s, m_f = 1])} \quad (34)$$

$$e^{-S_{\text{eff}}[L_s = \infty, m_f]} = \langle 0_H | \mathcal{O}(m_f) | 0_H \rangle^2 \quad (35)$$

The chiral condensate operator is:

$$\bar{\psi}\psi = -\frac{1}{2V} \sum_x \sum_{i=1}^2 [\bar{\psi}_R^i(x) \psi_L^i(x) + \bar{\psi}_L^i(x) \psi_R^i(x)] \quad (36)$$

The following observable is related to the chiral condensate in a background gauge field:

$$\begin{aligned} P_1[L_s, m_f] &= \int [d\bar{\Psi} d\Psi] \bar{\psi}\psi e^{-S_F - S_{\text{eff}}^{PV}} \\ P_1[L_s, m_f] &= -\frac{1}{V} \sum_x [D_F^{-1}(x, L_s - 1, 2; x, 0, 2) + D_F^{-1}(x, 0, 1; x, L_s - 1, 1)] e^{-S_{\text{eff}}} \end{aligned} \quad (37)$$

$$P_1[L_s = \infty, m_f] = -\frac{1}{V} \sum_x [\langle 0_H | \hat{c}_x^\dagger \mathcal{O}(m_f) \hat{c}_x | 0_H \rangle \langle 0_H | \mathcal{O}(m_f) | 0_H \rangle + (c \rightarrow d)] \quad (38)$$

The t' Hooft vertex operator is:

$$w = \frac{1}{V} \sum_x \left[\prod_{i=1}^2 (\bar{\psi}_R^i(x) \psi_L^i(x)) + \prod_{i=1}^2 (\bar{\psi}_L^i(x) \psi_R^i(x)) \right] \quad (39)$$

The following observable is related to the t' Hooft vertex in a background gauge field:

$$\begin{aligned} P_2[L_s, m_f] &= \int [d\bar{\Psi} d\Psi] w e^{-S_F - S_{\text{eff}}^{PV}} \\ P_2[L_s, m_f] &= \frac{1}{V} \sum_x [D_F^{-2}(x, L_s - 1, 2; x, 0, 2) + D_F^{-2}(x, 0, 1; x, L_s - 1, 1)] e^{-S_{\text{eff}}} \end{aligned} \quad (40)$$

$$P_2[L_s = \infty, m_f] = \frac{1}{V} \sum_x [\langle 0_H | \hat{c}_x^\dagger \mathcal{O}(m_f) \hat{c}_x | 0_H \rangle^2 + (c \rightarrow d)] \quad (41)$$

The observables $e^{-S_{\text{eff}}}$, P_1 and P_2 are interesting because they correspond to Overlap expressions and, therefore, their values at the $L_s = \infty$ limit are calculable. Furthermore, these

quantities are sensitive to the topology of the background gauge field. The expectation value of the fermion condensate is:

$$\langle \bar{\psi} \psi \rangle = \frac{1}{Z} \int [dU] \int [d\bar{\Psi} d\Psi] \int [d\Phi^\dagger d\Phi] \bar{\psi} \psi e^{-S} \quad (42)$$

$$\langle \bar{\psi} \psi \rangle_{L_s=\infty} = \frac{\int dU \frac{1}{V} \sum_x \left[\langle 0_H | \hat{c}_x^\dagger \mathcal{O}(m_f) \hat{c}_x | 0_H \rangle \langle 0_H | \mathcal{O}(m_f) | 0_H \rangle + (c \rightarrow d) \right] e^{-S_G}}{\int dU \langle 0_H | \mathcal{O}(m_f) | 0_H \rangle^2 e^{-S_G}} \quad (43)$$

The expectation value of the t' Hooft vertex is:

$$\langle w \rangle = \frac{1}{Z} \int [dU] \int [d\bar{\Psi} d\Psi] \int [d\Phi^\dagger d\Phi] w e^{-S} \quad (44)$$

$$\langle w \rangle_{L_s=\infty} = \frac{\int dU \frac{1}{V} \sum_x \left[\langle 0_H | \hat{c}_x^\dagger \mathcal{O}(m_f) \hat{c}_x | 0_H \rangle^2 + (c \rightarrow d) \right] e^{-S_G}}{\int dU \langle 0_H | \mathcal{O}(m_f) | 0_H \rangle^2 e^{-S_G}} \quad (45)$$

Notice that a numerical evaluation of $\langle \bar{\psi} \psi \rangle_{L_s=\infty}$ and $\langle w \rangle_{L_s=\infty}$ requires two separate pure gauge simulations, one for the numerator and one for the denominator, i.e. the fermion determinant is treated as an observable [8], [7].

4 The free theory

In this section the propagator is given, its singular part is identified and the bare fermion mass which is a function of L_s, m_0, m_f , is extracted. As a verification of this result the smallest eigenvalue of the free $2n + 1$ dimensional Dirac operator is also calculated.

The propagator has been calculated for the infinite L_s case in the first reference of [6]. The propagator has also been calculated for the model described in section 2 but only in the limit where exponentially small contributions in L_s could be ignored [9]. The size of these contributions was alluded to but no explicit expression was given. Since in this paper the interest is on the behavior of these contributions, the full calculation is worked out. Because the general form of the propagator is the same as in [6], [9] an effort has been made to keep similar notation.

The free $2n + 1$ dimensional Dirac operator of eq. 7 in momentum space is:

$$D_F(p : s, s') = i\bar{p}\delta(s - s') - b(p)\delta(s - s') + \frac{1 + \gamma_5}{2}M(s, s') + \frac{1 - \gamma_5}{2}M^\dagger(s, s') \quad (46)$$

and

$$b(p) = \sum_{\mu=1}^{2n} [1 - \cos(p_\mu)] + 1 - m_0 \quad (47)$$

$$\bar{p}_\mu = \sin(p_\mu), \quad \mu = [1, \dots, 2n], \quad p_\mu = \frac{2\pi k_\mu}{L}, \quad k_\mu = [0, 1, \dots, L - 1] \quad (48)$$

$$M(s, s') = \delta(s + 1 - s') - \delta(s' - 0)\delta(L_s - 1 - s)(1 + m_f) \quad (49)$$

where the δ functions are understood as having “period” L_s . Notice that the first two terms of eq. 46 are the same as for Wilson fermions with mass $(1 - m_0)$, where $0 < m_0 < 1$ (see sect. 2). The second order free Dirac operator is diagonal in spin:

$$D_F D_F^\dagger = \frac{1 + \gamma_5}{2} \Omega_+ + \frac{1 - \gamma_5}{2} \Omega_- \quad (50)$$

where Ω_\pm have no spin indices and:

$$\begin{aligned} \Omega_+(p : s, s') &= [-b(p) + M(s, s')][-b(p) + M^\dagger(s, s')] + \bar{p}^2 \\ \Omega_-(p : s, s') &= \Omega_+(p : L_s - 1 - s, L_s - 1 - s') \end{aligned} \quad (51)$$

where:

$$\bar{p}^2 = \sum_{\mu=1}^{2n} \bar{p}_\mu^2 \quad (52)$$

The inverse of the second order free Dirac operator $D_F D_F^\dagger$ must therefore be of the form:

$$G = \frac{1 + \gamma_5}{2} G_+ + \frac{1 - \gamma_5}{2} G_-, \quad [D_F D_F^\dagger] G = I \quad (53)$$

where G_\pm have no spin indices. From general considerations G_\pm must be of the form [9]:

$$\begin{aligned} G_+(p : s, s') &= A_0 e^{-a|s-s'|} + A_1 e^{-a(s+s')} + A_2 e^{-a(L_s-1-s+L_s-1-s')} \\ &\quad + A_m [e^{-a(L_s-1+s-s')} + e^{-a(L_s-1+s'-s)}] \end{aligned} \quad (54)$$

$$G_-(p : s, s') = G_+(p : L_s - 1 - s, L_s - 1 - s') \quad (55)$$

The coefficients in eq. 55 are momentum dependent. The coefficient “a” is the solution of the equation:

$$\cosh(a) = \frac{1 + b^2 + \bar{p}^2}{2b} \quad (56)$$

A straight forward calculation results to the following expressions for the remaining coefficients:

$$A_0 = \frac{1}{2b \sinh(a)} \quad (57)$$

$$A_1 = -\frac{B}{\Delta} (b - e^{-a})(1 - m_f^2) \quad (58)$$

$$A_2 = \frac{B}{\Delta} (e^a - b)(1 - m_f^2) \quad (59)$$

$$A_m = -\frac{B}{\Delta} [2bm_f \sinh(a) + e^{-a(L_s-1)} (e^{-2a} [e^a - b] - m_f^2 [e^{-a} - b])] \quad (60)$$

where,

$$\begin{aligned} \Delta &= [e^{2a} (b - e^{-a}) + m_f^2 (e^a - b)] + [4m_f b \sinh(a)] e^{-a(L_s-1)} \\ &\quad + [m_f^2 (b - e^{-a}) + e^{-2a} (e^a - b)] e^{-2a(L_s-1)} \end{aligned} \quad (61)$$

In order to identify the singular part of the propagator an expansion in the variables p , m_f and $(1 - m_0)^{(L_s - 1)}$ is done treating these variables as numbers with magnitudes much smaller than one. The only singular amplitudes are A_2 and A_m and the resulting expression for the singular part of G_{\pm} is:

$$G_+^{\text{singular}}(p : s, s') = \frac{1}{p^2 + m_{\text{eff}}^2} \left\{ m_0(2 - m_0)e^{-a(L_s - 1 - s + L_s - 1 - s')} - m_{\text{eff}}(1 - m_0) \left[e^{-a(L_s - 1 + s - s')} + e^{-a(L_s - 1 + s' - s)} \right] \right\} \quad (62)$$

with,

$$m_{\text{eff}} = m_0(2 - m_0) \left[m_f + (1 - m_0)^{L_s} \right] \quad (63)$$

The expression for G_-^{singular} can be obtained from eq. 62 and 55. The propagator for the free theory is then given by:

$$D_F^{-1} = D_F^\dagger G \quad (64)$$

To verify the above result the smallest eigenvalue of $D_F D_F^\dagger$ is also calculated. The leading order term in an expansion as the one used above is:

$$\lambda_{\min} = p^2 + m_{\text{eff}}^2 + O(4) \quad (65)$$

and is proportional to the inverse of the singular part of G_{\pm} as it should be.

The interesting result of the above analysis is eq. 63. This is the mass of the lightest mode of the theory and is controlled by m_f , m_0 , L_s . This formula strongly suggests the pattern for chiral symmetry restoration in the model.

5 The Interacting Theory, General Considerations

The question on how the chiral symmetry restoration rate depends on the various parameters of the model ultimately can only be answered when the full theory is considered. This is done using numerical simulations in section 7. However, some general considerations that hint to the expected behavior are useful in order to guide the numerical experiments and to provide an understanding of the results. Such considerations leading to specific predictions are presented in this section. These predictions are confirmed by the numerical simulations and therefore sketch the mechanisms of chiral symmetry restoration in the model.

5.1 The Effects of Topology

In this section a special kind of trajectory [17], [6] that “cuts” through the various topological sectors of the configuration space is considered. The values of the relevant observables of section 3 are calculated along this trajectory.

Consider the following set of $U(1)$ gauge link U configurations labeled by the continuous parameter $\tau \in \mathfrak{R}$ [17], [6]:

$$\begin{aligned} U_1(n_1, n_2) &= \begin{cases} 1 & \text{if } n_1 \neq L - 1 \\ \exp \left[-i \frac{2\pi n_2}{L} \tau \right] & \text{if } n_1 = L - 1 \end{cases} \\ U_2(n_1, n_2) &= \exp \left[i \frac{2\pi n_1}{L^2} \tau \right] \end{aligned} \quad (66)$$

where U_1, U_2 are links defined on the sites n_1, n_2 of the two dimensional torus of size $L \times L$. This configuration is periodic along the second direction but has a discontinuity along the first. When τ is an integer the electric field strength is uniform $E = 2\pi\tau/L^2$. When τ is not an integer E has a discontinuity at $(n_1 - 1, n_2 - 1)$. The topological charge of the gauge field is defined as [16]:

$$q = \sum_p \frac{\log [U_p]}{2\pi i} \quad (67)$$

where the sum is over all plaquette variables U_p and the logarithm has $\log(1) = 0$ with the cut along the negative real axis. It is straightforward to verify that q is an integer that changes values as τ is varied between integer values (see figure 1). For more information on these configurations the reader is referred to [17], [6]. Here it is worthwhile to point out that this trajectory in configuration space is interesting because it connects the trivial configuration with uniform configurations that have non zero topological charge. As such, the configurations at integer τ can be thought of as local minima and therefore in some sense they represent vacua of different topological charge. The path that connects the configurations of integer τ is certainly not unique but it can nevertheless provide insightful information on how the transition between sectors of different topological charge takes place. Therefore, although one can not extract from this trajectory quantitative information, the qualitative information will be quite useful if, in particular, similar features are observed when the full configuration space is considered in the HMC simulation of the model in section 7.

In the following, the observables in equations 32 - 45 are considered in the presence of the gauge field configuration of eq. 66. The boundary conditions for both fermion flavors in the two dimensional space are taken to be antiperiodic. Of course, for the full dynamical $U(1)$ theory, the choice of boundary conditions is irrelevant for as long as they are the same for all flavors (they can change by $U(1)$ phases at the boundary).

The $L_s = \infty$ quantities are calculated using the Overlap formula. The finite L_s quantities are obtained by explicit computation of the determinants and inverses of D_F . The reader is reminded that $e^{-S_{\text{eff}}[L_s=\infty, m_f=0]}$ is not zero only in the topological sector $q = 0$. The quantity related to the chiral condensate $P_1[L_s = \infty, m_f = 0]$ is identically zero in all sectors. This is a consequence of the exact $SU(2)_L \times SU(2)_R$ chiral symmetry. Therefore a non zero $P_1[L_s, m_f = 0]$ at some finite L_s will indicate explicit breaking of the chiral symmetry. The quantity $P_2[L_s = \infty, m_f = 0]$ related to the t' Hooft vertex is not zero only in sectors $q = \pm 1$. This represents the anomalous breaking of the $U(1)$ axial symmetry.

In figure 1 the topological charge along with $S_G, S_{\text{eff}}^F, S_{\text{eff}}^{PV}, S_{\text{eff}}$ and $S_{\text{eff}} + S_G$ is shown for $L = 6, \mu l = 3.0, m_0 = 0.9, m_f = 0$, and $L_s = 14$ along the trajectory of eq. 66. The absolute scale in these figures is of course irrelevant. One can already see the separation of the different topological sectors with the $q = 0$ sector as the absolute minimum and the other sectors as relative minima. It is interesting to observe how the addition of S_{eff}^{PV} and S_G changes the fermion action S_{eff}^F .

In figure 2 S_{eff}, P_1 and P_2 are shown along the same trajectory and for the same parameters but for various values of L_s . In the S_{eff} figure at $\tau = 2$ the curves with larger S_{eff} correspond to larger L_s with $L_s = 4, 6, 8, 10, 12, 14$. The curve that sharply increases to ∞ at $\tau \sim 0.5$ corresponds to $L_s = \infty$. It is clear from this figure that in the $q = 0$ sector

the $L_s = \infty$ limit is approached very fast. The $q \neq 0$ sectors carry large actions relative to the $q = 0$ action and therefore they also approximate the $L_s = \infty$ limit very well. The only regions that suffer from a slow approach to the $L_s = \infty$ limit are the two regions in the immediate neighborhood where τ changes from 0 to ± 1 . There, the $L_s = \infty$ result raises discontinuously but the finite L_s results approach this discontinuous behavior slowly.

In the P_1 figure at $\tau = 0$ the curves with smaller P_1 correspond to larger L_s with $L_s = 4, 6, 8, 10, 12, 14$. The $L_s = \infty$ curve is identically zero for all τ and is not plotted. From this figure it is seen that P_1 in the non zero topological sectors is negligible even at $L_s = 4$. In the zero topological sector it decreases very fast with increasing L_s for all values of τ except for the same two regions where τ changes from 0 to ± 1 . There, two large spikes appear with heights that essentially do not change with increasing L_s . Instead, their width slowly shrinks with increasing L_s . As a result, chiral symmetry is slowly restored in these regions.

In the P_2 figure at $\tau = 1$, the curves with larger P_2 correspond to larger L_s with $L_s = 4, 6, 8, 10, 12, 14, \infty$. The $L_s = \infty$ curve can be distinguished by the discontinuous behavior at the places where q changes from 0 to ± 1 and from ± 1 to ± 2 . From this figure it is seen that P_2 approaches the $L_s = \infty$ limit very fast for all τ except again for the regions where q changes.

The slow approach of S_{eff} and P_2 to the $L_s = \infty$ limit in the regions of changing topological charge is not particularly troubling since the effect is a small percent of the values that they acquire along the trajectory. Not so for P_1 . The two “spikes” present a large size contribution to a quantity that should otherwise be identically zero. In figure 3 P_1 is plotted vs. L_s for various “cross sections” of figure 2. For $\tau = 0$ (diamonds) P_1 decays exponentially. For $\tau = 0.3, 0.4$ (squares, crosses) the rate of the exponential decay decreases. Finally, close to the point where the configuration changes topological charge, $\tau \approx 0.55$ (octagons), there is almost no decay at all.

The slow approach to the $L_s = \infty$ limit in the neighborhoods of changing topological charge q is expected. According to the topological charge definition eq. 29, q changes because the number of negative eigenvalues of the single particle Hamiltonian H of eq. 16 changes. Therefore, in that neighborhood there are configurations for which H has zero eigenvalues. These configurations were identified in [6] and also discussed in [10]. For these configurations the Overlap formulation is not well defined because the ground state is degenerate and, in turn, the finite L_s theory experiences large correlations along the $2n + 1$ dimension. However, the set of configurations for which H has an exact zero eigenvalue is of measure zero. As a result the Overlap is a well defined formulation. On the other hand regions of the configuration space surrounding these special configurations are characterized by small decay rates. The importance of these regions is determined dynamically and only a full simulation of the theory can accurately probe their effect to the exponential decay. However, close to the continuum limit one would expect that these regions are severely suppressed since the pure gauge action separates sectors with topological charge that differs by one unit with barriers of energy $\sim 1/g_0^2$ (see S_G in figure 1). But away from the continuum limit, where most numerical simulations are performed, these regions may become important and contribute to the explicit breaking of chiral symmetry.

In order to gain some understanding about this mode of chiral symmetry breaking the expectation value of the chiral condensate $\langle \bar{\psi} \psi \rangle$, eq. 42, was calculated in a configuration

space restricted only on the trajectory of eq. 66. It is plotted vs. L_s in figure 4 for an $L = 6$ lattice, $m_0 = 0.9$, $m_f = 0$ and various gauge couplings $\mu l/L$, $\mu l = 3.0, 2.5, 2.0, 1.5, 1.0$ (diamonds, squares, crosses, octagons, stars). For $\mu l = 3.0$ there is exponential decay with a fast rate until $L_s = 10$. For $L_s = 12$ and above there still is exponential decay but with a smaller rate. As the gauge coupling is decreased the inflection point moves to larger L_s and the slower of the two rates becomes faster until at $\mu l = 1.0$ there is no visible inflection below $L_s = 18$. This phenomenon can be easily understood by looking at P_1 in figure 2 ($\mu l = 3.0$ there). For L_s smaller than about 10 the explicit breaking that occurs inside the $q = 0$ sector dominates and the contribution of the “spikes” to the expectation value is small by comparison. When this breaking has almost completely disappeared, $L_s > 10$, the breaking that comes from the “spikes” dominates. This breaking disappears at a slower rate as the width of the “spikes” shrinks. However, as the gauge coupling is decreased the regions of changing topology where the “spikes” are located are weighted less by the pure gauge action and the slower rate approaches the initial faster rate.

Therefore, one sees that there are two distinct mechanisms that control the restoration rate of chiral symmetry. One is related to the restoration in the $q = 0$ topological sector. The other is related to the topology changing regions of the gauge field configuration space and in particular to the regions that connect the $q = 0$ and $q = \pm 1$ sectors.

To conclude this section the effects of m_f are presented. The observable P_1 along the trajectory of eq. 66 is plotted in figure 5 for $L = 6$, $\mu l = 3.0$, $m_0 = 0.9$, $m_f = 0.1$ and $L_s = 4, 6, 8, 10, 12, 14, 16, \infty$. At $\tau = 0$ the curves with larger P_1 correspond to larger L_s . It is clear that the $L_s = \infty$ limit is approached rapidly and with no complications. Again the region of changing topology approaches the $L_s \rightarrow \infty$ limit slowly but it is away from it only by a small percentage. One would expect that the non zero m_f behavior will persist down to some small value of m_f before signs of the $m_f = 0$ behavior described above appear. One can visualize how figure 5 changes with decreasing m_f . As m_f becomes smaller P_1 tends to zero in the various topological sectors. However, its value, at the place where the topological charge changes from 0 to ± 1 , remains roughly constant resulting in the spikes of figure 2 .

In order to see more clearly how the $L_s = \infty$ limit is approached for $m_f = 0.1$, the expectation value of the chiral condensate $\langle \bar{\psi} \psi \rangle$, eq. 42, is calculated in a configuration space restricted only on the trajectory of eq. 66 for various L_s and for $L_s = \infty$. In figure 6 $[\langle \bar{\psi} \psi \rangle_{L_s} - \langle \bar{\psi} \psi \rangle_{\infty}] / \langle \bar{\psi} \psi \rangle_{L_s}$ is plotted vs. L_s . Again, one can see that there is an inflection at about $L_s = 10$. However, when the inflection occurs the $L_s = \infty$ value has already being approached to better than 0.3%. This behavior is encouraging as far as numerical simulations are concerned. Since most numerical simulations are done for small but non zero masses one would expect that for some range of masses the effects of the topology changing configurations to these simulations will generally be small and perhaps even lost in the statistical noise.

5.2 The Effects of Gauge Field Fluctuations

In this section the effects of gauge field fluctuations to the chiral symmetry restoration rate are discussed.

The two mechanisms of chiral symmetry restoration identified in section 5.1 will be

affected when the gauge field is allowed to fluctuate. The effect of dynamical gauge fields to the mechanism that restores chiral symmetry in the zero topological sector can be seen by measuring $\langle \bar{\psi}\psi \rangle$ in an ensemble of configurations generated by applying small fluctuations to the trivial configuration. In particular, consider gauge field configurations with links $U = e^{ir\pi}$ where r is a random number in the range $-\epsilon < r < \epsilon$ with ϵ a small number that controls the size of the fluctuations. These configurations have a “flat” distribution and in this ensemble $\langle \bar{\psi}\psi \rangle$ is obtained by calculating $\langle P_1 \rangle / \langle e^{-S_{\text{eff}}} \rangle$. In figure 7 $\langle \bar{\psi}\psi \rangle$ is plotted vs. L_s for various values of $\epsilon = 0.4, 0.3, 0.2, 0.1$ and 0.01 corresponding to octagons, stars, squares, crosses, and diamonds. The value at each point was calculated in an ensemble consisting of 40 configurations. Antiperiodic boundary conditions have been used for the fermions and $L = 6$, $m_f = 0$, $m_0 = 0.9$. It can be seen that as the size of the fluctuations decreases the chiral symmetry restoration rate increases.

Some insight to this behavior can be gained by considering the following “heuristic” argument. The Dirac operator of equation 7 can be rewritten as:

$$\begin{aligned} D_F &= \not{D}_{\text{naive}} + \mathcal{M} \\ \not{D}_{\text{naive}}(x, x') &= \frac{1}{2} \sum_{\mu} \gamma_{\mu} \left[U_{\mu}(x) \delta(x + \hat{\mu} - x') - U_{\mu}^{\dagger}(x') \delta(x' + \hat{\mu} - x) \right] \\ \mathcal{M} &= -B + \frac{1 + \gamma_5}{2} M + \frac{1 - \gamma_5}{2} M^{\dagger} \end{aligned} \quad (68)$$

where B is the Hermitian matrix given in eq. 17 and M is given by equation 49. For the free theory in momentum space $D_F = i\vec{p} + \mathcal{M}(p)$ where $\mathcal{M}(p)$ can be read from eq. 46. One can think of $\mathcal{M}(p)$ as being a momentum dependent mass matrix. The smallest eigenvalue of $\mathcal{M}\mathcal{M}^{\dagger}$ is obtained at zero momentum and is equal to m_{eff}^2 with $m_{\text{eff}} = m_0(2 - m_0) [m_f + (1 - m_0)^{L_s}]$, eq. 63. The quantity $(1 - m_0)$ is the smallest eigenvalue of the matrix B . When interactions are turned on the smallest eigenvalue of B will shift to values $(1 - m'_0)$ larger than the free theory $(1 - m_0)$ value for the simple reason that the matrices $U_{\mu}(x) \delta(x + \mu - x')$ that make up B are unitary. Therefore, the smallest eigenvalue of $\mathcal{M}\mathcal{M}^{\dagger}$ will now be m'_{eff}^2 , $m'_{\text{eff}} = m'_0(2 - m'_0) [m_f + (1 - m'_0)^{L_s}]$. For small fluctuations one may still be able to think of \mathcal{M} as a mass matrix. If that is the case the lightest mass in the theory will be m'_{eff} and one sees that for $m_f = 0$ the chiral symmetry restoration rate will become faster as the fluctuations become smaller.

Finally, the quantitative effect of dynamical gauge fields to the mechanism related to topology changing is complicated since it involves some understanding about the volume of configuration space that contains gauge field configurations for which the Overlap Hamiltonian has near zero eigenvalues. As already mentioned, one would expect that this volume will shrink as the continuum limit is approached because the pure gauge action introduces energy barriers of size $\sim 1/g_0^2$ between sectors with topological charge that differs by one unit.

5.3 The range of m_0

In this section the allowed range of m_0 and the effects it has in the approach to the continuum limit are discussed.

In order for the doubler species to acquire masses of the order of the cutoff m_0 must be in the range $0 < m_0 < 2$ [4]. As it was found in [6], in order for the transfer matrix to be positive definite for all gauge fields, the range of m_0 should be further restricted to $0 < m_0 < 1$, eq. 11. For QCD, any value of m_0 in this range should lead to the same continuum limit since the local and global symmetries of the theory remain unchanged. On the other hand, different choices of m_0 , will result in different ways of approaching this limit. For the Schwinger model there is an additional complication. As mentioned in the introduction, a four-Fermi term is a marginal operator in two dimensions. Although it is not explicitly introduced in the action, the DWF regularization introduces such a term with a coefficient that depends on m_0 [8], [7]. Therefore, different values of m_0 will lead to different continuum limits. For this reason, a quantitative study of the effects of m_0 to the approach to the continuum limit in the Schwinger model is complicated and will not be done here. However, there are some important generic features that can be discussed.

Consider the Overlap Hamiltonian H , eq. 16 as a function of the $2n + 1$ dimensional mass μ [6]. It is easy to see that for $\mu = -\infty$, H has the same number of positive and negative eigenvalues, $N_+ = N_-$. It is also easy to see that for $\mu < 0$, H can not have a zero eigenvalue. As a result H has $q = 0$, for $\mu < 0$. As μ is increased from zero, H can develop zero eigenvalues and as a result $q \neq 0$ (eigenvalues cross zero altering N_-). Close to the continuum it can be easily seen that most crossings will occur around $\mu = 0$ [6]. Farther away from the continuum pure gauge numerical simulations [18] show a finite region $[\mu_{\min}, \mu_{\max}]$ where most crossings occur. This suggests that one should keep $\mu_{\max} \ll m_0$ for two reasons. First, one would like to be as far away as possible from the region where crossings occur since, as discussed in section 5.1, it is there that the decay rates become small. Second, as can be seen from the definition of the topological charge, eq. 29, it is only then that the full effects of non-trivial topology are visible to the fermions. In particular, one would expect that by keeping $\mu_{\max} < m_0$ quantities that are sensitive to topology will have a “smoother” approach to the continuum limit.

From the above discussion it appears that at any coupling the safest choice would be to set m_0 to its largest allowed value $m_0 \approx 1$. Even then, because in general $0 < \mu_{\min} < \mu_{\max} < 2$ it may be that far away from the continuum $1 < \mu_{\max} \Rightarrow m_0 < \mu_{\max}$. If this situation occurs the finite lattice spacing errors at that coupling will be large and the chiral symmetry restoration rate will be slow. However, the numerical simulations of [18] indicate that even for reasonably strong couplings $\mu_{\max} < 1$. The couplings used in this paper fall in this category (see figure 1 in [18]) and m_0 is kept fixed to $m_0 = 0.9$.

In [13] it was found that for QCD some tuning ($m_0 = 1.7$) was necessary in order to sufficiently restore chiral symmetry at $L_s = 10$. However, the configurations used there were not generated with the DWF action but rather with the staggered fermion action at $\beta = 5.7$. It is possible that this large value of m_0 is at least due in part to the “semi-quenched” nature of the calculation and if the configurations are generated with the DWF action setting $m_0 \approx 1$ may be sufficient.

6 Dynamical Simulation of the Massive Theory with the Overlap

In this section a full dynamical simulation that measures the chiral condensate $\langle \bar{\psi}\psi \rangle$ and the t' Hooft vertex $\langle w \rangle$ of the two flavor massive Schwinger model using the Overlap formalism of the model of section 2 will be presented. The result is interesting on its own right and it also provides the $L_s = \infty$ numbers that will be used to compare with the results of the dynamical simulation for finite L_s presented in the next section.

The expectation values $\langle \bar{\psi}\psi \rangle$ and $\langle w \rangle$ can be calculated numerically using equations 43 and 45 respectively. As it is evident from these equations a pure gauge simulation with action S_G must be performed with the overlap factors appearing in the numerator and denominator treated as observables. The pure gauge theory expectation values of the overlap factors in the numerator and denominator are then divided to produce $\langle \bar{\psi}\psi \rangle$ or $\langle w \rangle$. A heat bath algorithm was used to generate configurations with the standard Wilson plaquette pure gauge action of eq. 3.

Measurements of $\langle w \rangle$ for the massless, $m_f = 0$, theory were performed in [8]. The reader is referred there for more details on the method and results. However, the result for w in that reference can not be compared directly with the $m_f = 0$ result here since a different implementation of the Overlap was used. Furthermore, the single plaquette action used there was a heat kernel action while the standard Wilson plaquette action is used here. The result for $\langle w \rangle / m_\gamma^2$ vs. L_s on an $L = 6$, $m_0 = 0.9$, $\mu l = 3.0$ lattice is given in figure 8. This quantity acquires a non zero vacuum expectation value even for $m_f = 0$ (dotted lines) as a result of the anomalously broken $U(1)$ axial symmetry.

The result for $\langle \bar{\psi}\psi \rangle / m_\gamma$ vs. m_f on the same lattice and for the same parameters is presented in figure 9. The behavior of $\langle \bar{\psi}\psi \rangle$ vs. m_f is interesting in that $\langle \bar{\psi}\psi \rangle \sim m_f$ for $m_f < 0.1$ while $\langle \bar{\psi}\psi \rangle \sim m_f^{1/3}$ for $m_f > 0.1$. Fits to Am_f^p for $m_f < 0.1$ and for $m_f > 0.1$ are shown in the same figure. Both fits have a χ^2 per degree of freedom of about one. For $m_f < 0.1$ $p = 0.996(3)$ while for $m_f > 0.1$ $p = 0.32(2)$.

This type of behavior was found by analytical continuum calculations in [19]. In particular, the linear behavior was found to take place for $m_f L \ll 1$ while the $m_f^{1/3}$ behavior was found to occur for $m_f L \gg 1$. Unfortunately, the coefficients calculated in that reference can not be directly compared with the ones here because, as previously discussed, an additional four-Fermi interaction is induced by the DWF regularization [8], [7]. This term in two dimensions is not irrelevant and it will contribute to the continuum limit. For the same reasons the value of $\langle w \rangle$ can not be directly compared with the continuum results of [19].

7 Hybrid Monte Carlo Simulation

In this section a full dynamical simulation of the two flavor Schwinger model for finite L_s is presented. The algorithm used is the standard Hybrid Monte Carlo (HMC) algorithm [20]. The expectation value of the chiral condensate $\langle \bar{\psi}\psi \rangle$, eq. 42, is calculated and used to monitor the amount of explicit chiral symmetry breaking. The reason for using

$\langle \bar{\psi}\psi \rangle$ instead of the pion mass is that in two dimensions there is no spontaneous chiral symmetry breaking and although the pion mass vanishes for vanishing fermion mass the pion is not a Goldstone particle. In this sense $\langle \bar{\psi}\psi \rangle$ is as good a probe of chiral symmetry breaking as is the pion mass, but unlike the pion mass it has the practical advantage of not requiring large lattice size along the time direction in order to measure the decay of the pion correlator. The effects of the anomalously broken $U(1)$ axial symmetry are monitored by measuring the expectation value of the t' Hooft vertex $\langle w \rangle$, eq. 44.

The smaller size lattices were simulated on the workstations of the Physics Department of Columbia University. The larger lattices were simulated on the Silicon Graphics Power Challenge Array computer system at NCSA UIUC and also on the C90 supercomputer at PSC.

7.1 The algorithm

The HMC Hamiltonian is given by:

$$\begin{aligned} H_{\text{HMC}} = & \frac{1}{2}P^2 + S_G[U] + \chi^\dagger \left(D_F^\dagger[m_f, L_s] D_F[m_f, L_s] \right)^{-1} \chi \\ & + \Phi^\dagger \left(D_F^\dagger[m_f = 1, L_s] D_F[m_f = 1, L_s] \right) \Phi \end{aligned} \quad (69)$$

where P is the HMC momentum, S_G is the pure gauge plaquette action given in eq. 3, U is the $U(1)$ gauge field, χ is the pseudofermion field, Φ is the bosonic PV field and D_F is the three dimensional Dirac operator of eq. 7.

The HMC trajectory length τ is set to $\tau = 1$, the step size is τ/N and the number of steps N is adjusted according to the size of the effective bare fermion mass. Typical simulations with $m_f \geq 0.05$ are done with 50 HMC steps. For the $m_f = 0$ simulations the number of steps is set to $100 - 400$ depending on the size of L_s . This is necessary because, for $m_f = 0$, trajectories that cross between different topological sectors experience large HMC fermion forces (for more details see section 7.2). The Conjugate Gradient residual is set to 10^{-8} . Typically, the number of Conjugate Gradient iterations is around 50 and does not exceed ~ 100 for $m_f = 0$ and $L_s = 14$. The number of measurements is $\sim 8,000$ except for the more “expensive” 12×12 , $10 < L_s$ lattices where $1,000 - 2,000$ measurements were performed.

7.2 HMC and topology

In this section problems related to the sampling of non zero topological sectors with the HMC algorithm at small fermion masses are discussed.

The HMC algorithm is very successful provided the fermion mass does not become very small. If the fermion mass becomes very small then the effects of topology are not reproduced correctly. In particular, the measurement of $\langle w \rangle$ becomes problematic. If, for some fixed volume, the fermion mass is made very small then similar analysis as in [21] indicates that the effect of the zero modes coming from different topological sectors becomes important. In particular, as can be seen from the Overlap implementation [6], [8], at finite physical volume, at zero mass and in the $L_s \rightarrow \infty$ limit, the operator w

receives contributions only from sectors ± 1 , while the fermion Boltzman weight (fermion determinant) is not zero only in sector 0. As m_f is turned on (and/or L_s is decreased from infinity) the fermionic determinant becomes non zero in sectors other than 0 and the operator w receives contributions from sectors other than ± 1 . Because of this behavior at small fermion mass the HMC algorithm will mostly sample the sector 0 where the observable w receives small contributions. The algorithm will infrequently visit the sectors ± 1 , but when it does the observable w will receive large contributions to “make up” for the small sampling rate. As a result, when the fermion mass is decreased a larger number of HMC iterations will be needed to sample the ± 1 sectors correctly. Therefore, for a fixed amount of computer time, if the fermion mass becomes very small the important contributions may not even be sampled at all and as a result not only the expectation value of w will be underestimated but also the associated error. This type of difficulty has already been noticed in simulations of the Schwinger model [22], [12].

The problem described above leaves a clear signature in the time history of w . In figure 10 the time history of w is given for six different fermion masses at $L_s = 14$. As the fermion mass is decreased, the average around which w fluctuates decreases. This decrease is compensated by the large contributions received from the $q = \pm 1$ sectors. These contributions start to appear as “spikes” in the time history. The smaller the fermion mass the larger the “height” of the spikes but since the corresponding Boltzman weight becomes smaller their frequency also decreases. Notice the different scale of the $m_f = 0.05$ and $m_f = 0.0$ graphs.

But it is not only $\langle w \rangle$ that is affected at small fermion masses. If, along an HMC trajectory, the topological charge changes then the fermion determinant changes by a large amount. As a result, the HMC fermion force becomes large and the HMC step size errors become large. Therefore, as the fermion mass is made smaller one must adjust the HMC step size accordingly. Finally, it should be stressed that these difficulties are not related to DWF but rather to the HMC algorithm. In particular, the simulations using the overlap in section 6 do not suffer from these problems since there the fermion determinant is treated as an observable in a pure gauge heat bath.

7.3 $m_f = 0$

In this section a strict test of chiral symmetry restoration is done.

A full dynamical simulation using the HMC algorithm is performed with the explicit fermion mass m_f set to zero so that the only breaking of chiral symmetry comes from the finite extent L_s . The restoration rate at fixed physical volume and various lattice spacings is studied by measuring $\langle \bar{\psi} \psi \rangle$ for various values of L_s . Although this provides a strict test one must keep in mind that the non-zero topological sectors may be suppressed more than they should for the reasons mentioned in section 7.2. This means that the rate of restoration of chiral symmetry observed here is mainly due to effects that occur in the zero topological sector and its vicinity. The following results were obtained at fixed $m_0 = 0.9$.

In figure 11, $\langle \bar{\psi} \psi \rangle / m_\gamma$ is plotted in a “log” plot vs. L_s at fixed physical volume $\mu l = 3.0$ and for various lattice spacings $\mu l / L = \mu a$ where $L = 6, 8, 10, 12$ corresponding to the lines from top to bottom. Data for $L = 4$, $L_s = 6 - 10$ are statistically indistinguishable from the $L = 6$ data and are not plotted. For $L_s = 6 - 10$ the decay is exponential with

a rate that becomes faster as the lattice spacing decreases. For $L_s = 12 - 22$ the decay is again exponential but with a slower rate. Again this rate becomes faster as the lattice spacing decreases. Also, the percent change of the rate at $L = 6$ is $\approx 54 \pm 6\%$ but at $L = 12$ is $\approx 31 \pm 6\%$. The fits shown are two parameter fits to $\langle \bar{\psi}\psi \rangle / m_\gamma = Be^{-cL_s}$. The χ^2 per degree of freedom is smaller than one for all the fits except for the $L = 12$, $L_s = 6 - 10$ data that have a χ^2 per degree of freedom of ≈ 3 .

The exponentiated rate e^{-c} of the various fits vs. $1/L \sim a$ is shown in figure 12. The diamonds correspond to the $L_s = 6 - 10$ fits while the crosses to the $L_s = 10 - 22$ fits. One can see that e^{-c} is roughly a linear function of $1/L \sim a$ for the $L_s = 6 - 10$ fits and for $L = 8, 10, 12$. However, more data at smaller lattice spacings are needed before one can be confident that scaling has set in and that this is the correct scaling form.

The facts that the rate changes for $10 < L_s$, that the slower rate approaches the faster one as the continuum limit is approached and that both rates become faster as the continuum limit is approached can all be understood from the analysis in sections 5.1 and 5.2. Finally, the t' Hooft vertex $\langle w \rangle$ was also measured but, as expected from the discussion in section 7.2, its value and associated error is underestimated. In particular, its value is much lower than the corresponding Overlap value of section 6. For this reason that data is uninteresting and is not presented here.

7.4 $\mathbf{m_f} \neq \mathbf{0}$

In this section the $m_f \neq 0$ case is studied. Since typical QCD simulations are done for non zero fermion mass the results of this section are of practical interest.

Dynamical simulations are performed with masses m_f large enough, $0.1 \leq m_f$, so that the effects of topological sectors $q = 0, \pm 1$ are not miscalculated due to problems associated with the HMC algorithm as described in section 7.2. Both $\langle \bar{\psi}\psi \rangle$ and $\langle w \rangle$ are measured and their approach to the $L_s = \infty$ limit is studied and compared with the $L_s = \infty$ results of section 6. This is done for fixed physical volume, and various lattice spacings. The parameter m_0 is kept fixed at 0.9.

In figure 13 $\left[\langle \bar{\psi}\psi \rangle / m_\gamma \right]^3$ is plotted vs. L_s for $m_f = 0.1, 0, 2, 0.3, 0.5$ at fixed physical volume and lattice spacing, $\mu l = 3.0$, $L = 6$. According to the results in section 6 one expects that $\left[\langle \bar{\psi}\psi \rangle / m_\gamma \right]^3 \sim m_{\text{eff}}$. Therefore a fit of $\left[\langle \bar{\psi}\psi \rangle / m_\gamma \right]^3$ vs. L_s is made to the form $A + Be^{-cL_s}$. All fits have a χ^2 per degree of freedom $\approx 1 - 2$. In these figures the cross is the coefficient A and the dotted lines are the $L_s = \infty$ result of figure 9 plus/minus the error. One can see that as m_f becomes larger the $L_s = \infty$ result is approached faster. This is in accordance with naive expectations born out from the free theory formula for m_{eff} eq. 63.

In figure 14 $\langle w \rangle / m_\gamma^2$ is plotted vs. L_s for the same parameters as in figure 13. The fits are again to a form $A + Be^{-cL_s}$. One can see that the $L_s = \infty$ result has already been approached at $L_s = 6$.

The effects of changing the lattice spacing at $m_f = 0.2$ can be seen in figures 15 and 16. In figure 15 $\left[\langle \bar{\psi}\psi \rangle / m_\gamma \right]^3$ is plotted vs. L_s at fixed physical volume $\mu l = 3.0$ for different lattice spacings $\mu l / L = \mu a$, $L = 4, 6, 8, 10$. The fits are again to a form $A + Be^{-cL_s}$ and have a χ^2 per degree of freedom of $\approx 1 - 2$. One can see a similar behavior as the one in

section 7.3. As the lattice spacing is reduced the rate c of the exponential approach to the $L_s = \infty$ result increases. For example, $\langle \bar{\psi}\psi \rangle$ at the larger lattice spacing $L = 4$ decays with $c = 0.54(3)$ but at the smaller lattice spacing $L = 10$ it decays faster with $c = 1.1(1)$. However, one should note that for $L = 8$ and $L = 10$ the rate saturates and is essentially dictated by the $L_s = 4, 6$ points with the $L_s = 6$ point very close to the $L_s = \infty$ result. If a second slower rate sets in for $10 \lesssim L_s$ it is unimportant and is lost in the statistical noise. This can be understood from the analysis at the end of section 5.1 (in particular see figure 6). Similar behavior is observed in figure 16 for $\langle w \rangle / m_\gamma^2$.

Finally, similar results are obtained if one keeps the physical volume and m_f in physical units fixed while changing the lattice spacing. This can be seen in figures 17 and 18 by comparing the $L = 10, m_f = 0.2$ data (diamonds) with data at $L = 4, m_f = 0.5$ (squares). In these graphs the physical volume is fixed at $\mu l = 3.0$, and m_f in physical units is fixed at $m_f L = 2.0$. Again the decay rate increases as the lattice spacing is reduced. $\langle \bar{\psi}\psi \rangle$ at the larger lattice spacing $L = 4$ decays with $c = 0.48(5)$ but at the smaller lattice spacing $L = 10$ decays faster with $c = 1.1(1)$.

8 Conclusions

In this paper the properties of Domain Wall Fermions (DWF) were studied in the context of the two flavor Lattice Schwinger model. The expectation value of the chiral condensate $\langle \bar{\psi}\psi \rangle$ was used to probe issues related to restoration of the regularization induced chiral symmetry breaking. The expectation value of the relevant t' Hooft vertex $\langle w \rangle$ was used to probe issues related to topology.

Dynamical numerical simulations of the full theory were performed and it was found that, as expected from perturbative considerations, the restoration of chiral symmetry at a fixed physical volume and lattice spacing is exponentially fast with increasing L_s where L_s is the size in lattice units of the $2n + 1$ direction. In particular, it was found that chiral symmetry is restored with an exponential rate for L_s up to some value and with a slower exponential rate for L_s above that value. For the range of lattice spacings used in this paper the inflection appeared at $L_s \approx 10$. It was found that the first rate is associated with restoration of chiral symmetry in the zero topological sector while the second slower rate is associated with the regions of gauge field configuration space that connect the $q = 0$ and $q = \pm 1$ topological sectors.

The effects of the size of the lattice spacing a to the two restoration rates were studied using both analytical arguments and explicit numerical simulations of the full theory. It was found that for zero explicit fermion mass the rate associated with the zero topological sector becomes faster as the lattice spacing is decreased. The chiral condensate vanishes like e^{-cL_s} with e^{-c} being roughly a linear function of a , but more data at smaller lattice spacings are needed before one can be confident that scaling has set in and that this is the correct scaling form. The second slower rate also becomes faster as the lattice spacing is decreased and it differs less from the faster rate as the lattice spacing becomes smaller. For the smallest lattice spacing studied it differed by $\approx 31 \pm 2\%$.

For small but non zero explicit fermion mass m_f the values of $\langle \bar{\psi}\psi \rangle$ and $\langle w \rangle$ were measured. The corresponding $L_s = \infty$ numbers were calculated by performing numerical

simulations with the Overlap formalism. It was found that the $L_s = \infty$ numbers were also approached exponentially with a rate that became faster as the lattice spacing decreased. Furthermore, the larger the fermion mass the sooner the $L_s = \infty$ value was approached and for the fermion masses studied in this paper the $L_s = \infty$ result was already achieved to within a few percent at $L_s = 4 - 8$. If a second slower rate does set in for $10 \lesssim L_s$, it is unimportant and was lost in the statistical noise. Finally, an interesting result was obtained from the measurements of $\langle \bar{\psi}\psi \rangle$ and $\langle w \rangle$ vs. m_f . It was found that these measurements are in agreement with the analytical predictions of [19]. In particular the interesting $\langle \bar{\psi}\psi \rangle \sim m_f^{1/3}$ behavior was reproduced.

The next step is to carry out a similar investigation for dynamical QCD. Many of the characteristics of DWF found here are sufficiently generic so that one would expect that they will also be present in QCD. If it turns out that QCD at the presently accessible lattice spacings, volumes and quark masses has similar restoration rates as the ones found here, then DWF will indeed provide a powerful fermion discretization method.

Acknowledgments

The author would like to thank N. Christ, R. Mawhinney, R. Narayanan and H. Neuberger for many useful discussions. This research was supported in part by the DOE under grant # DE-FG02-92ER40699. This work was also partially supported by the National Center for Supercomputing Applications under grant # PHY970002N and utilized the Silicon Graphics Power Challenge Array computer system at the National Center for Supercomputing Applications, University of Illinois at Urbana-Champaign. Also, this research was supported in part by grant # PHY960005P from the Pittsburgh Supercomputing Center and utilized the C90 supercomputer.

References

- [1] K.G. Wilson, New Phenomena in Subnuclear Physics, ed. A Zichichi (Plenum Press, New York), Part A, (1975), 69.
- [2] J. Kogut, L. Susskind, Phys. Rev. **D11** (1975) 395; Banks, J. Kogut, L. Susskind, Phys. Rev. **D13** (1976) 1043; L. Susskind, Phys. Rev. **D16** (1977) 3031.
- [3] A. Ukawa, Nucl. Phys. B (Proc. Suppl.) **53** (1997) 106.
- [4] D.B. Kaplan, Phys. Lett. B 288 (1992) 342; Nucl. Phys. B (Proc. Suppl.) **30** (1993) 597.
- [5] R. Narayanan, Nucl. Phys. B (Proc. Suppl.) **34** (1994) 95; M. Creutz, Nucl. Phys. B (Proc. Suppl.) **42** (1995) 56; Y. Shamir, Nucl. Phys. B (Proc. Suppl.) **47** (1996) 212.
- [6] R. Narayanan, H. Neuberger, Phys. Lett. B **302** (1993) 62; Phys. Rev. Lett. **71** (1993) 3251; Nucl. Phys. B **412** (1994) 574; Nucl. Phys. B **443** (1995) 305.

- [7] R. Narayanan, H. Neuberger, Phys. Lett. B **380** (1996) 291; Nucl. Phys. B **477** (1996) 521; Nucl. Phys. B (Proc. Suppl.) **53** (1997) 658; Nucl. Phys. B (Proc. Suppl.) **53** (1997) 661; Phys. Lett. B **393** (1997) 360; [heplat/9705006](#).
- [8] R. Narayanan, H. Neuberger and P. Vranas, Phys. Lett. B **353** (1995) 507; Nucl. Phys. B (Proc. Suppl.) **47** (1996) 596.
- [9] Y. Shamir, Nucl. Phys. B **406** (1993) 90.
- [10] V. Furman, Y. Shamir, Nucl. Phys. B **439** (1995) 54.
- [11] A. Jaster, DESY-96-083, [hep-lat/9605011](#).
- [12] P.M. Vranas, Nucl. Phys. B (Proc. Suppl.) **53** (1997) 278;
- [13] T. Blum, A. Soni [hep-lat/9611030](#).
- [14] D. Boyanovsky, E. Dagatto and E. Fradkin, Nucl. Phys. B **285** (1987) 340.
- [15] A. Dettki, I. Sachs and A. Wipf, ETH-TH-93, [hep-th/9310085](#).
- [16] C. Panagiotakopoulos, Nucl. Phys. B **251** (1985) 61.
- [17] J. Smit, J. Vink, Nucl. Phys. B **286** (1987) 485.
- [18] R. Narayanan and P. Vranas, [heplat/9702005](#).
- [19] A.V. Smilga, Phys. Lett. B **278** (1992) 371; J.E. Hetrick, Y. Hosotani, and S. Iso, Phys. Lett. B **350** (1995) 92.
- [20] S. Duane, A.D. Kennedy, B.J. Pendleton, D. Roweth, Phys. Lett. **195 B** (1987) 216.
- [21] H. Leutwyler, A. Smilga, Phys. Rev D **46** (1992) 5607.
- [22] F. Fucito and S. Solomon, Phys. Lett. B314 (1984) 230; M.L. Laursen, J. Smit, and J.C. Vink, Phys. Lett. B262 (1991) 467; H. Dilger Phys. Lett. B294 (1992) 263, Nucl. Phys. B434 (1995) 321, Int. J. Mod. Phys. C6 (1995) 123; U.J. Wiese, Nucl. Phys. B318 (1989) 153;

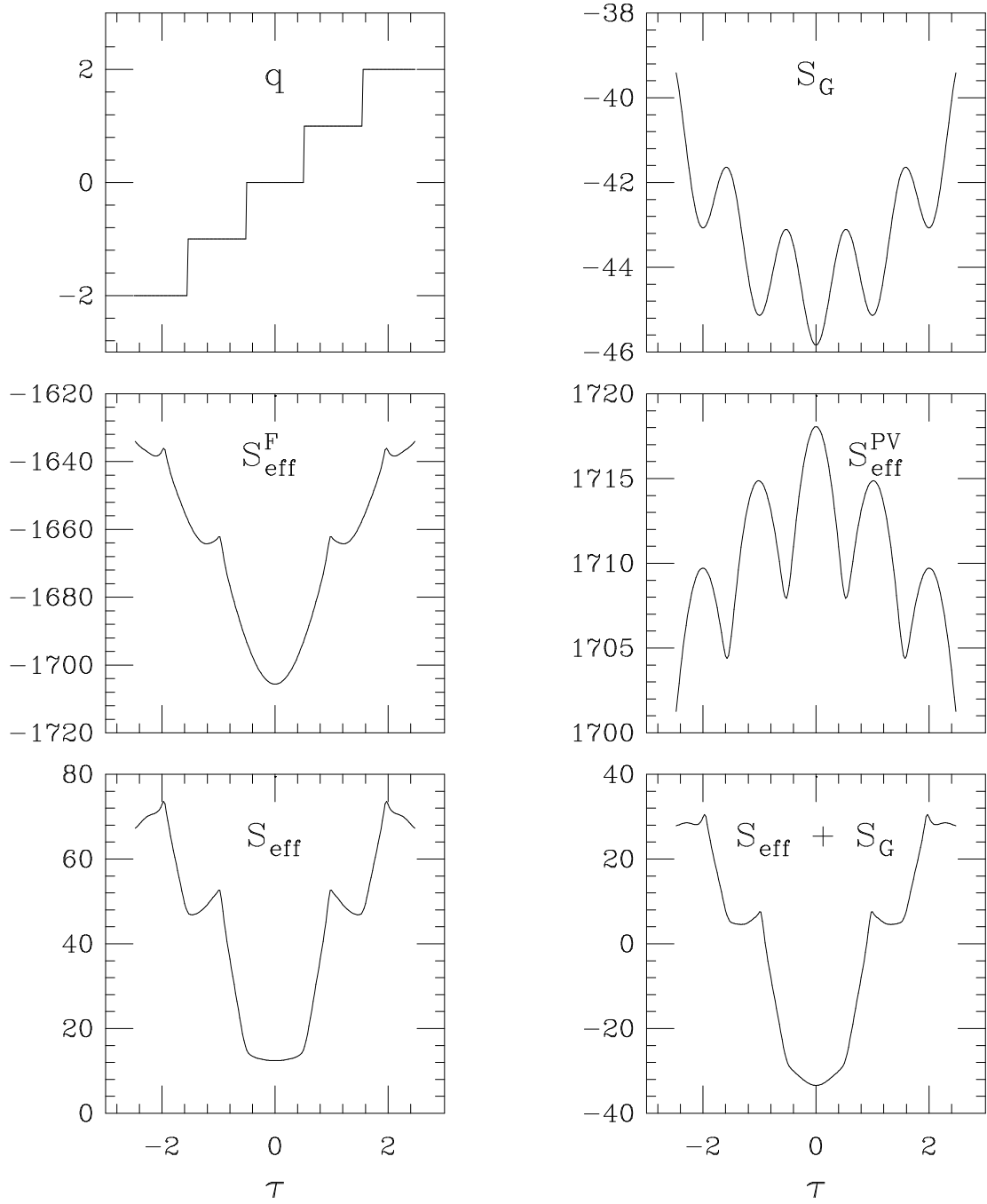


Figure 1. Observables (for definitions see section 3) along the configuration space trajectory, eq. 66, labeled by τ . The parameters have values: $L = 6$, $\mu l = 3.0$, $m_0 = 0.9$, $m_f = 0$, $L_s = 14$.

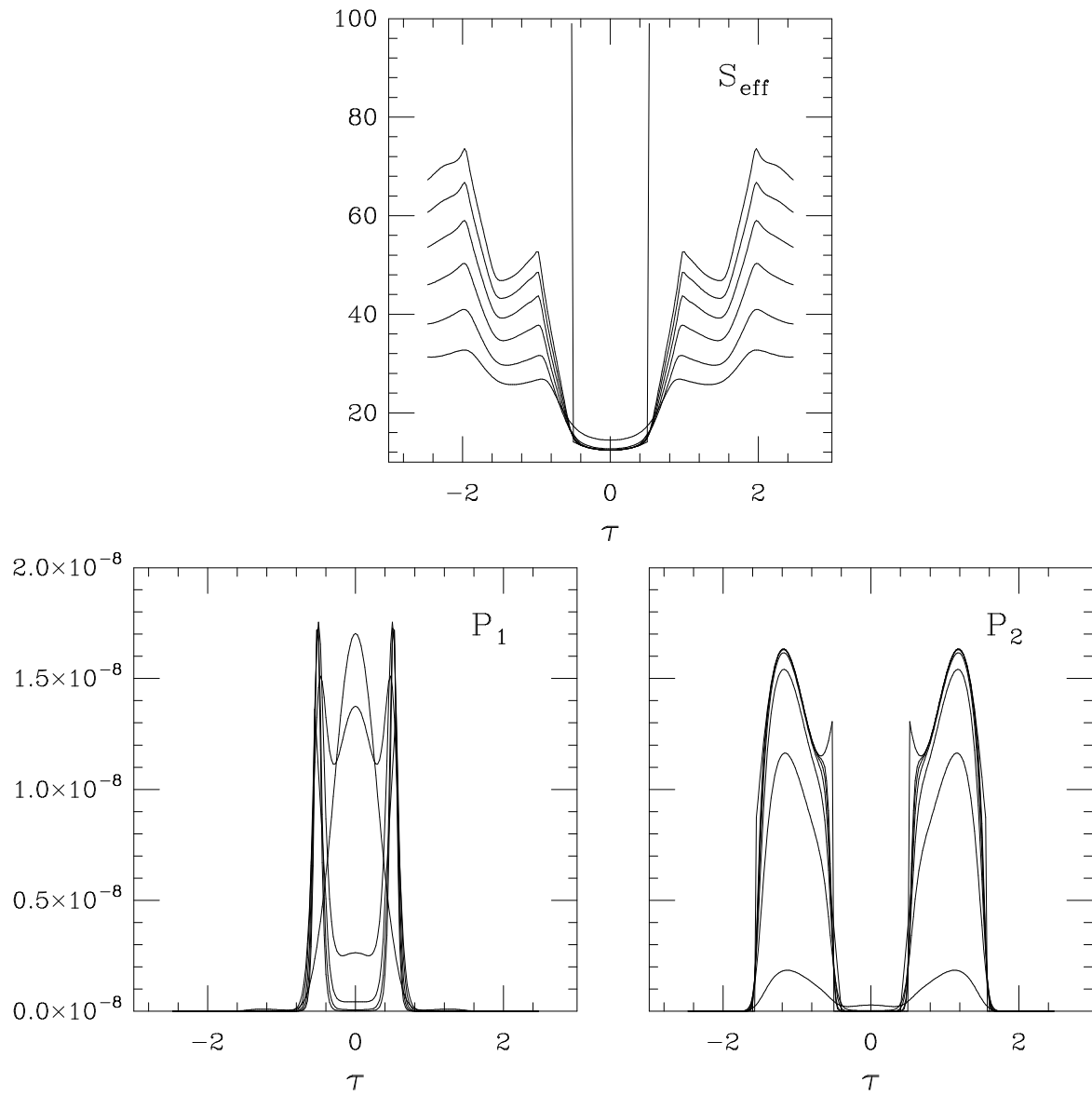


Figure 2. Observables (for definitions see section 3) along the configuration space trajectory, eq. 66, labeled by τ . The parameters have values: $L = 6$, $\mu l = 3.0$, $m_0 = 0.9$, $m_f = 0$, $L_s = 4, 6, 8, 10, 12, 14, \infty$. At $L_s = \infty$ $P_1 = 0$.

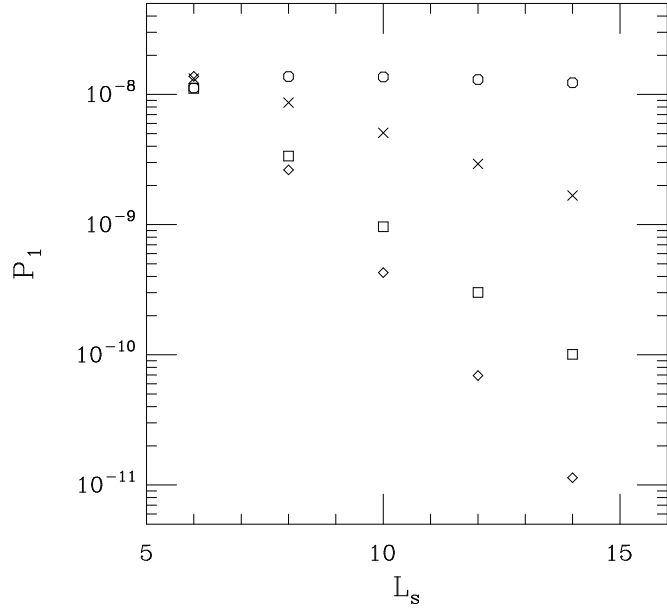


Figure 3. P_1 from fig. 2 vs. L_s at different values of $\tau = 0, 0.3, 0.4, 0.55$ corresponding to diamonds, squares, crosses, octagons.

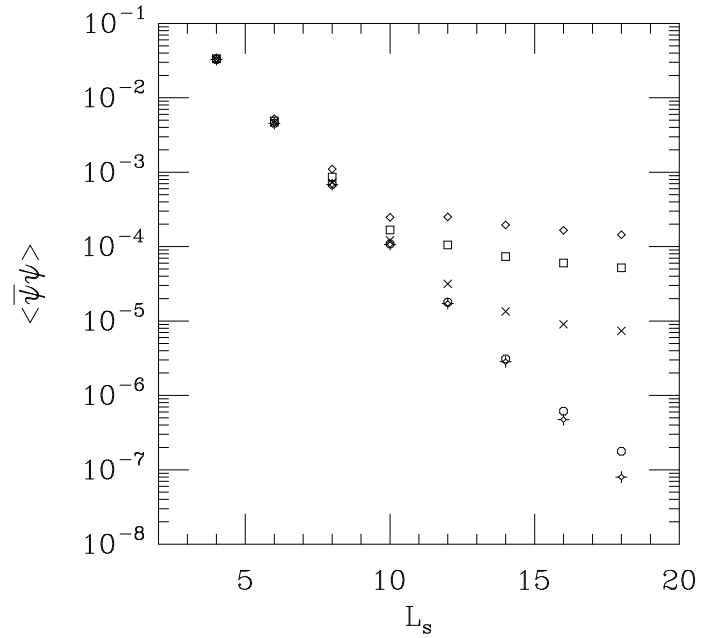


Figure 4. Expectation value of the chiral condensate in a configuration space restricted on the trajectory of eq. 66 vs. L_s for different gauge couplings. The parameters have values: $L = 6$, $m_0 = 0.9$, $m_f = 0$, $\mu l = 3.0, 2.5, 2.0, 1.5$, and 1.0 corresponding to diamonds, squares, crosses, octagons, and stars.

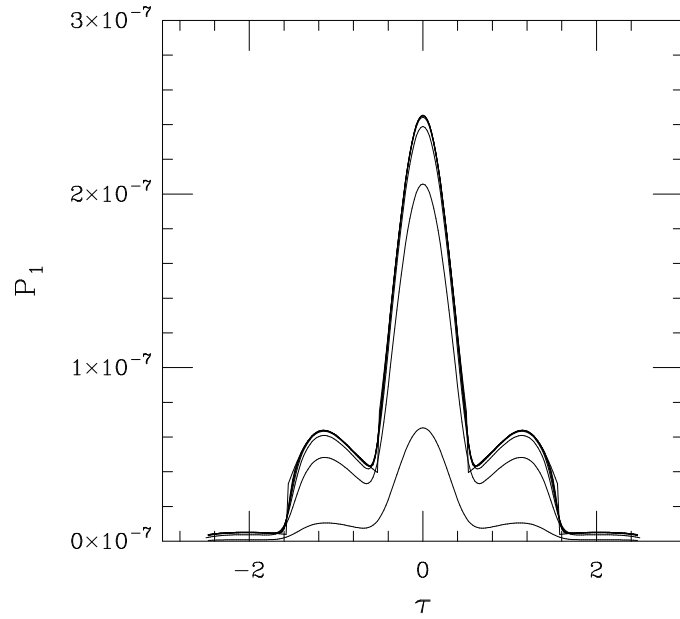


Figure 5. P_1 along the configuration space trajectory, eq. 66, labeled by τ . The parameters have values: $L = 6$, $\mu l = 3.0$, $m_0 = 0.9$, $m_f = 0.1$, $L_s = 4, 6, 8, 10, 12, 14, 16, \infty$.

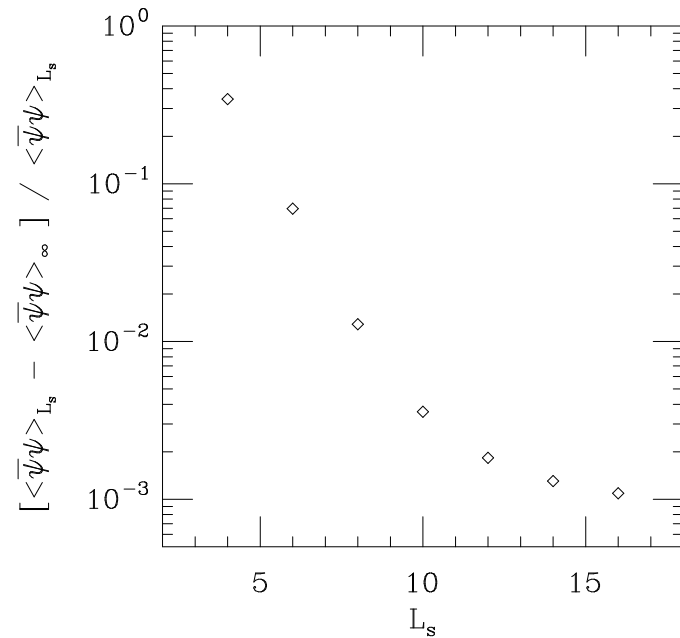


Figure 6. $[\langle \bar{\psi} \psi \rangle_{L_s} - \langle \bar{\psi} \psi \rangle_\infty] / \langle \bar{\psi} \psi \rangle_{L_s}$ vs. L_s for $m_f = 0.1$. $\langle \bar{\psi} \psi \rangle$ is the chiral condensate in a configuration space restricted on the trajectory of eq. 66. The parameters have values: $L = 6$, $\mu l = 3.0$, and $m_0 = 0.9$.

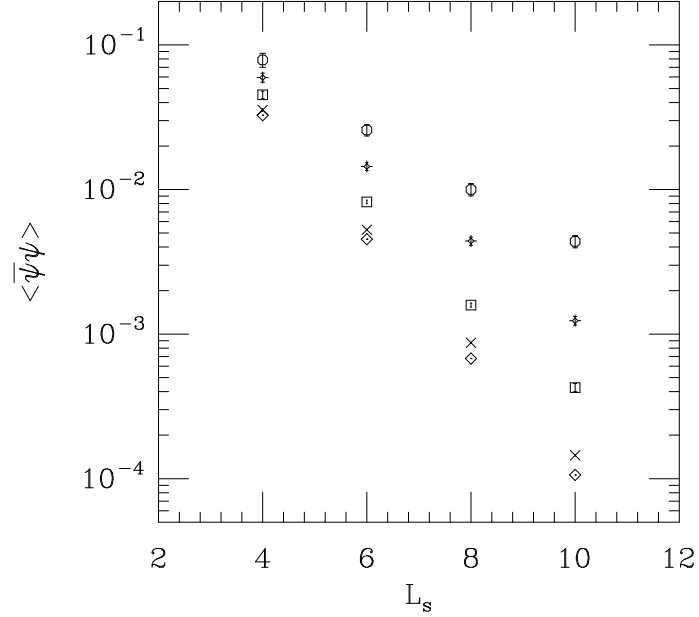


Figure 7. $\langle \bar{\psi} \psi \rangle$ vs. L_s calculated in an ensemble of configurations generated by applying small fluctuations of size ϵ to the trivial configuration ($U = e^{ir\pi}$ with r randomly distributed in $-\epsilon < r < \epsilon$). The parameters have values: $L = 6$, $m_0 = 0.9$, $m_f = 0$, $\epsilon = 0.4, 0.3, 0.2, 0.1$ and 0.01 corresponding to octagons, stars, squares, crosses, and diamonds.

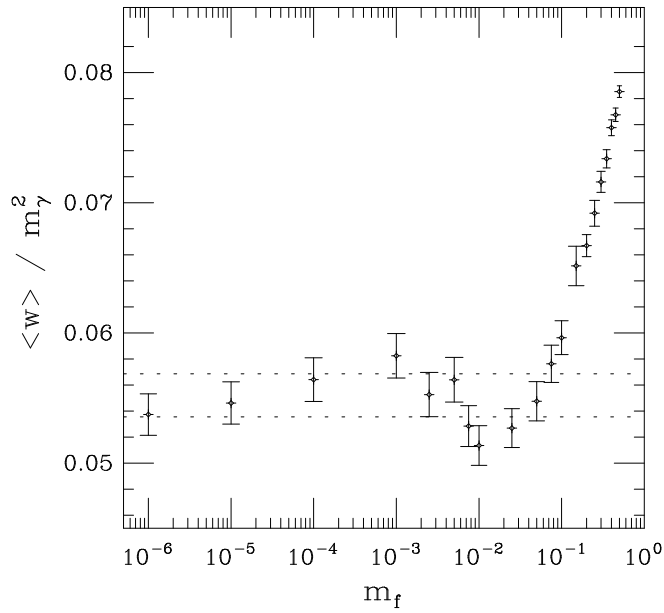


Figure 8. $\langle w \rangle / m_\gamma^2$ vs. m_f for $L = 6$, $m_0 = 0.9$, $\mu l = 3.0$ using the Overlap. The dotted lines are the $m_f = 0$ result \pm the corresponding statistical error.

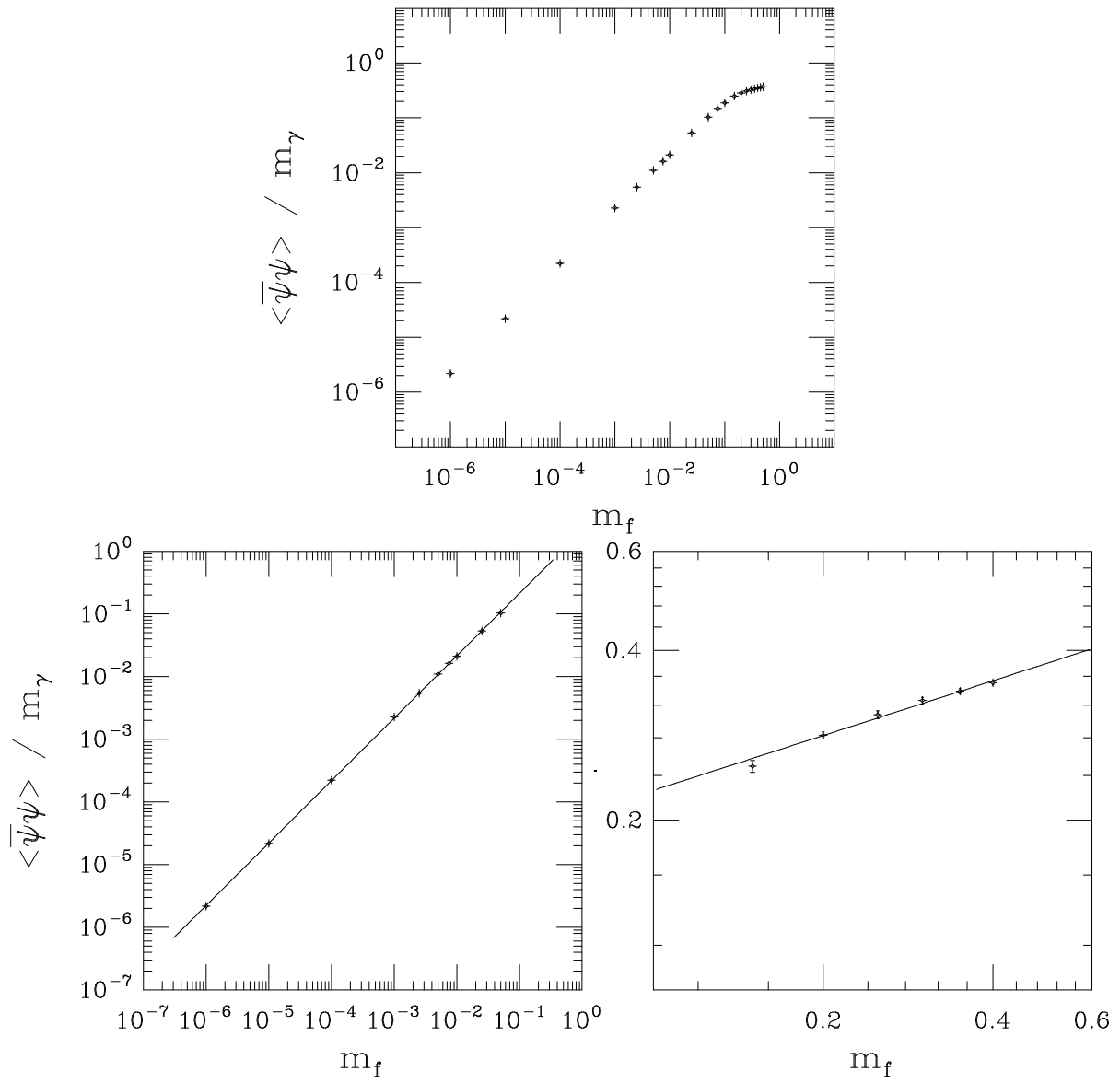


Figure 9. $\langle \bar{\psi} \psi \rangle / m_\gamma$ vs. m_f for $L = 6$, $m_0 = 0.9$, $\mu l = 3.0$ using the Overlap. The fits are to $\langle \bar{\psi} \psi \rangle = A m_f^p$. Both fits have a χ^2 per degree of freedom of about one. For $m_f < 0.1$ $p = 0.996(3)$, while for $m_f > 0.1$ $p = 0.32(2)$.

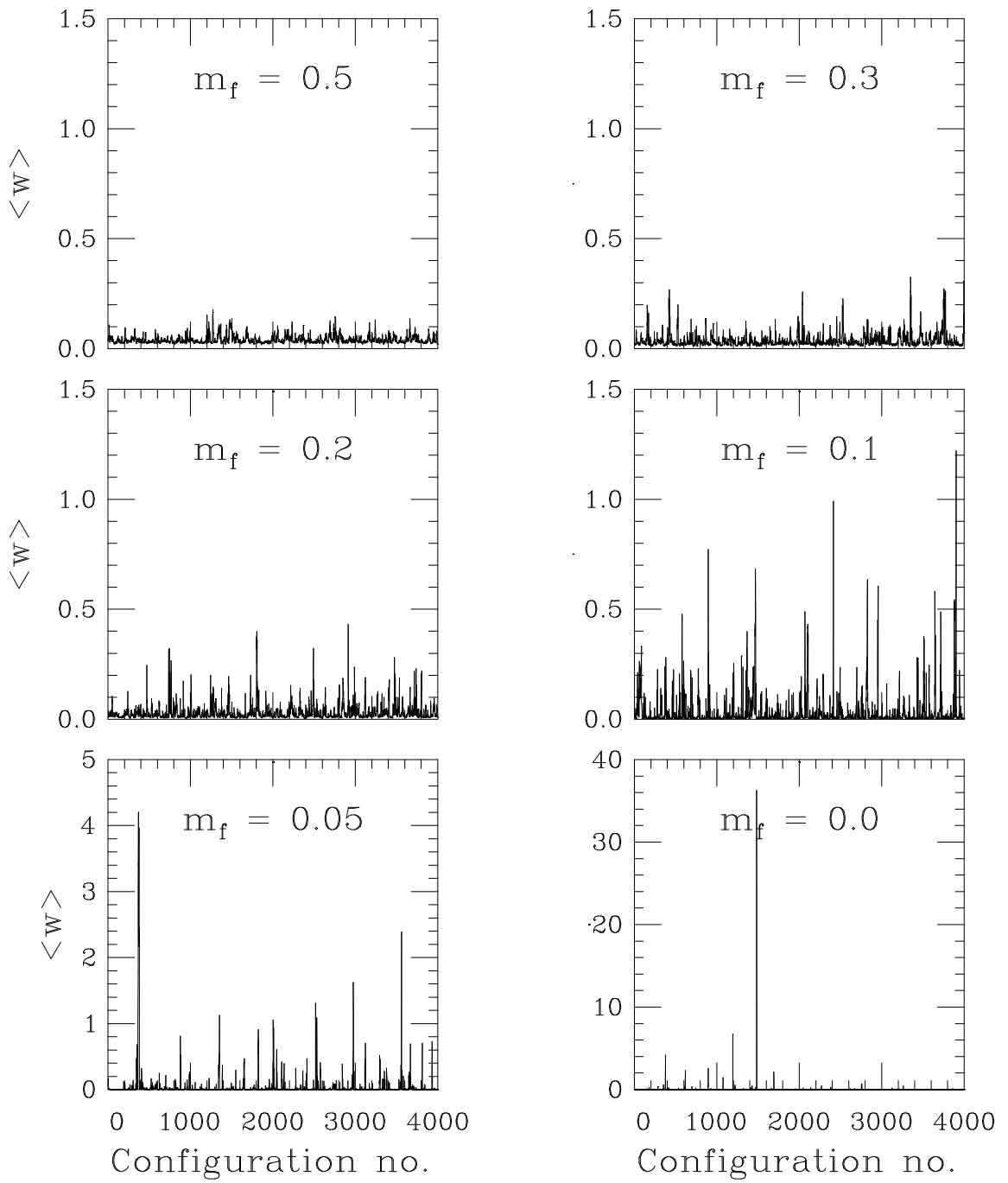


Figure 10. Time history of w , eq. 44, for six different values of m_f . Notice the different scale of the $m_f = 0.05$ and $m_f = 0.0$ graphs. The parameters are $L = 6$, $\mu l = 3.0$, $m_0 = 0.9$ and $L_s = 14$.

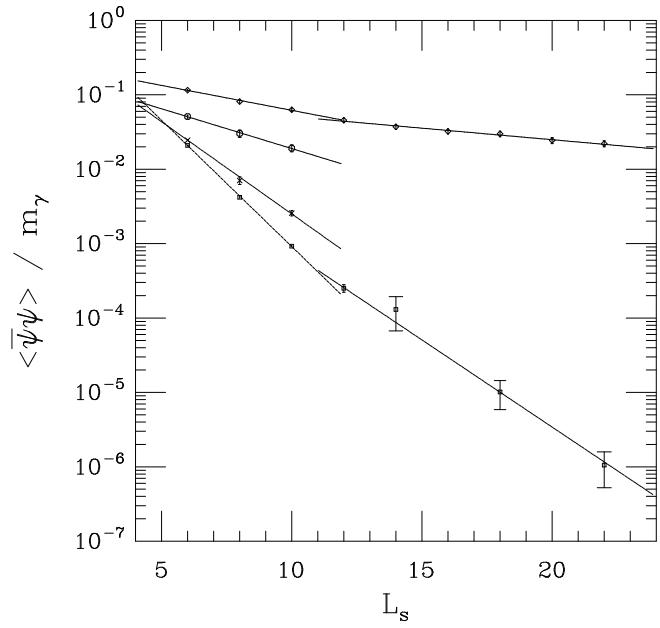


Figure 11. $\langle \bar{\psi} \psi \rangle / m_\gamma$, eq. 42, vs. L_s for $m_f = 0$, fixed physical volume $\mu l = 3.0$, $m_0 = 0.9$ and for four different lattice spacings $\mu l / L = \mu a$, with $L = 6, 8, 10, 12$ corresponding to the lines from top to bottom.

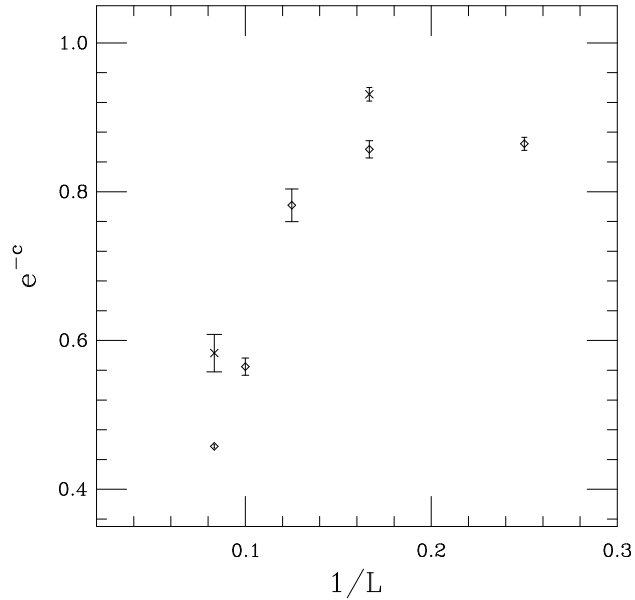


Figure 12. The exponentiated slopes, e^{-c} , of the lines in figure 11 vs. $1/L \sim a$. The diamonds correspond to the faster rates $6 \leq L_s \leq 10$ while the crosses to the slower ones $12 \leq L_s \leq 22$.

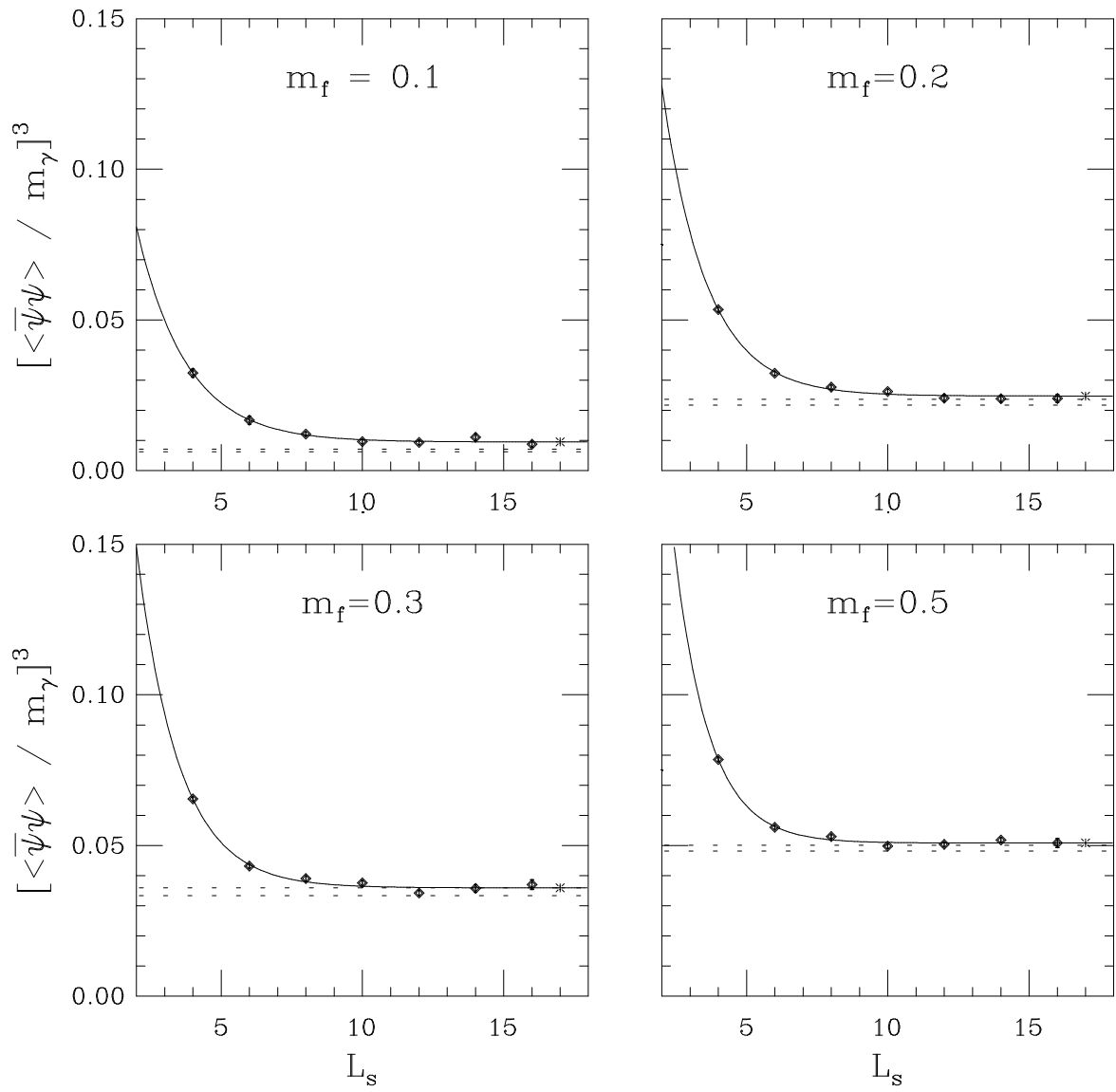


Figure 13. $[\langle \bar{\psi}\psi \rangle / m_\gamma]^3$ vs. L_s for four different m_f . The physical volume is fixed at $\mu l = 3.0$, $m_0 = 0.9$ and the lattice spacing is set by $L = 6$. The fits are to a function $A + Be^{-cL_s}$. The dotted line is the $L_s = \infty$ result \pm the error from figure 9. The cross is the coefficient A .

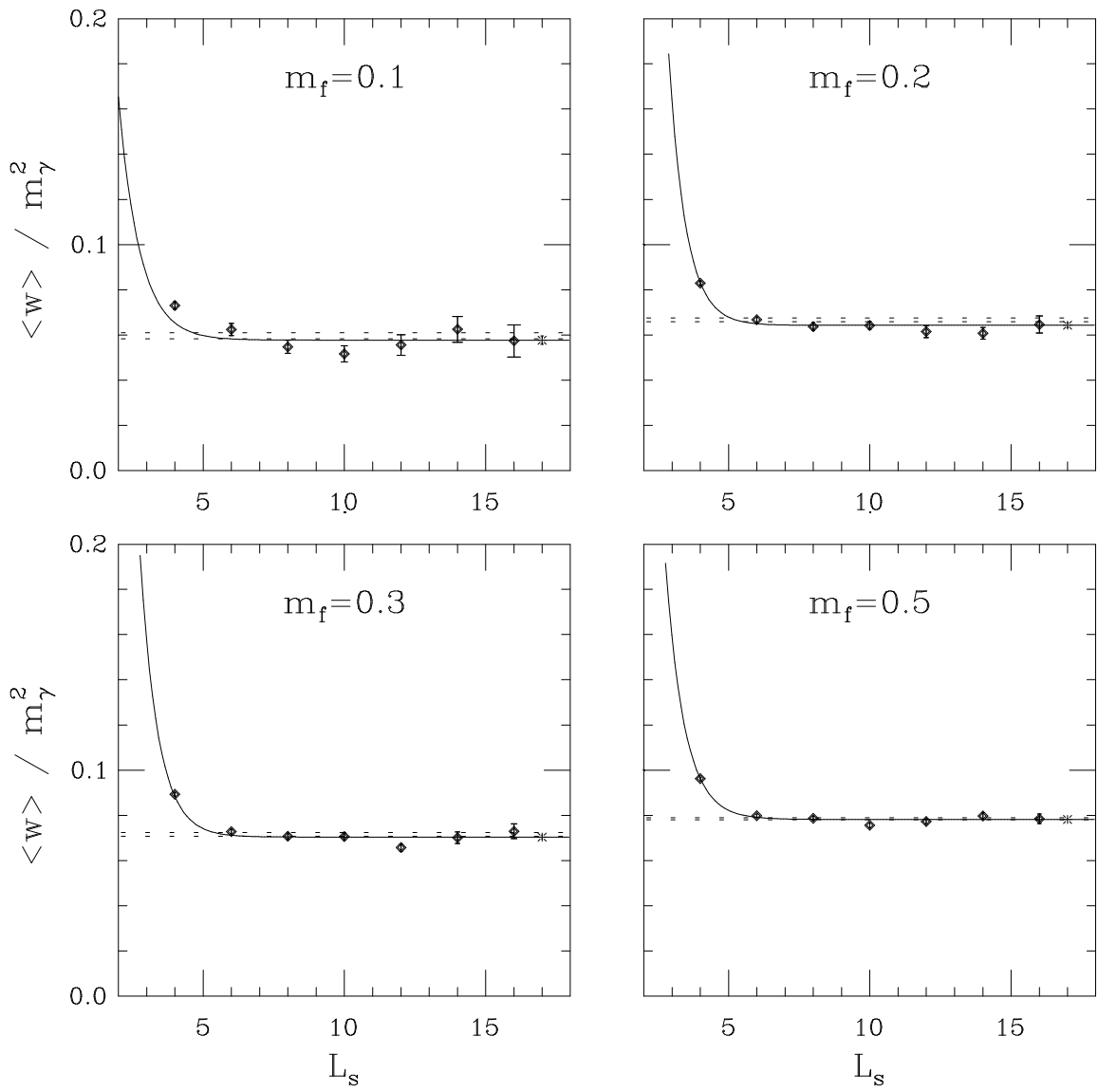


Figure 14. $\langle w \rangle / m_\gamma^2$ vs. L_s for four different m_f . The physical volume is fixed at $\mu l = 3.0$, $m_0 = 0.9$ and the lattice spacing is set by $L = 6$. The fits are to a function $A + Be^{-cL_s}$. The dotted line is the $L_s = \infty$ result \pm the error from figure 8. The cross is the coefficient A .

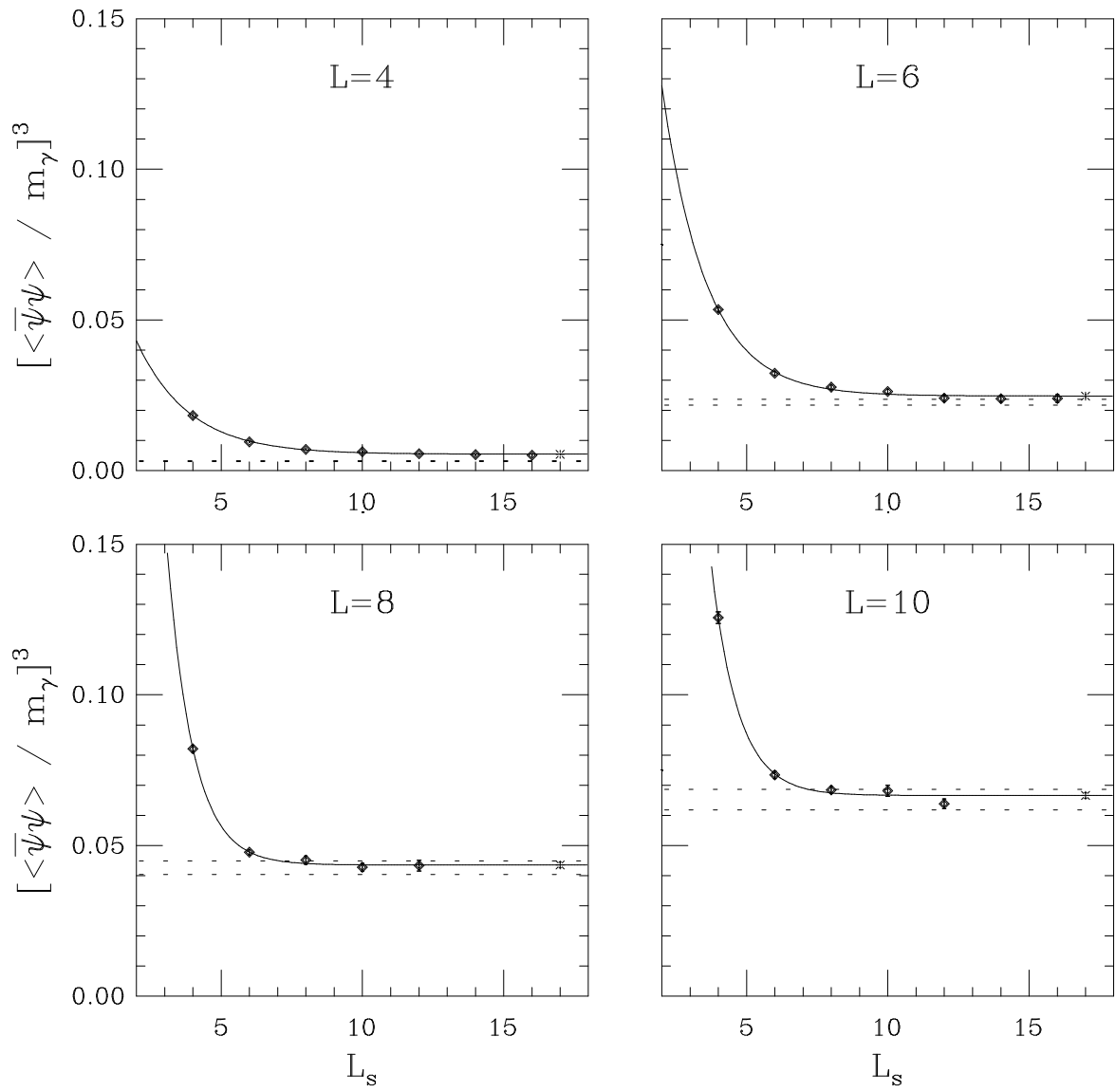


Figure 15. $[\langle \bar{\psi}\psi \rangle / m_\gamma]^3$ vs. L_s for four different lattice spacings set by L at fixed $m_f = 0.2$. The physical volume is fixed at $\mu l = 3.0$ and $m_0 = 0.9$. The fits are to a function $A + Be^{-cL_s}$. The dotted line is the $L_s = \infty$ result \pm the error. The cross is the coefficient A .

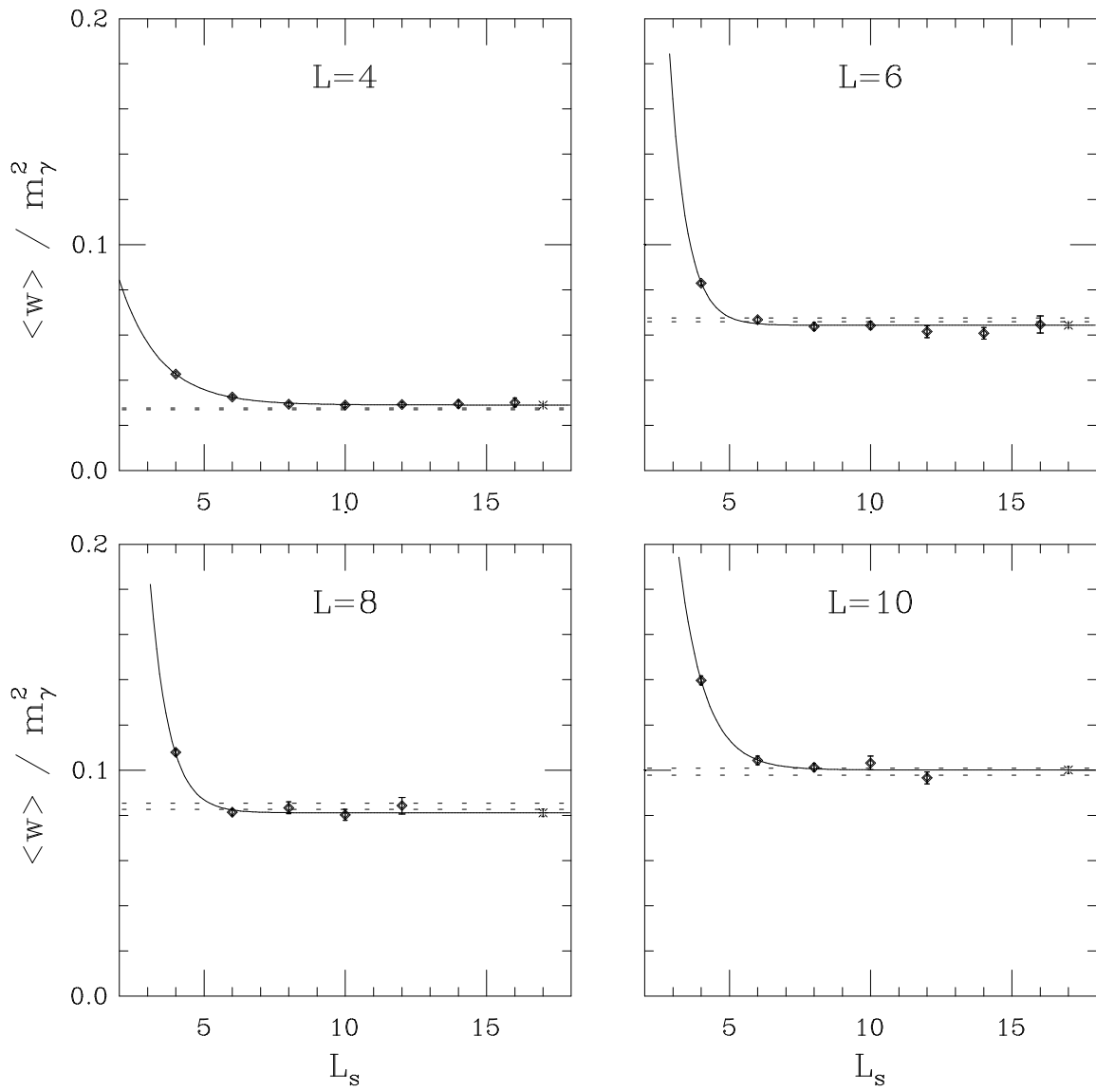


Figure 16. $\langle w \rangle / m_\gamma^2$ vs. L_s for four different lattice spacings set by L at fixed $m_f = 0.2$. The physical volume is fixed at $\mu l = 3.0$ and $m_0 = 0.9$. The fits are to a function $A + Be^{-cL_s}$. The dotted line is the $L_s = \infty$ result \pm the error. The cross is the coefficient A .

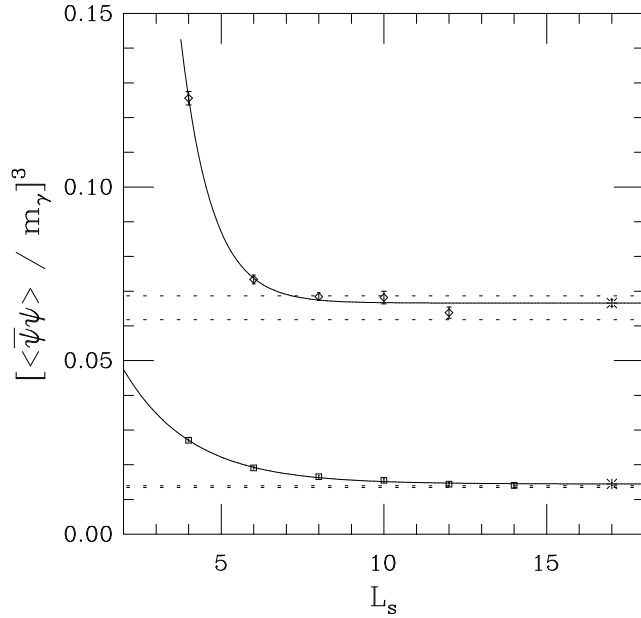


Figure 17. $[\langle \bar{\psi}\psi \rangle / m_\gamma]^3$ vs. L_s for two different lattice spacings set by $L = 4$ (squares) and $L = 10$ (diamonds) at $m_0 = 0.9$. The physical volume and $m_f L$ are fixed at $\mu l = 3.0$ and $m_f L = 2.0$. The fits are to $A + Be^{-cL_s}$. The dotted lines are the $L_s = \infty$ results \pm the error. The cross is the coefficient A .

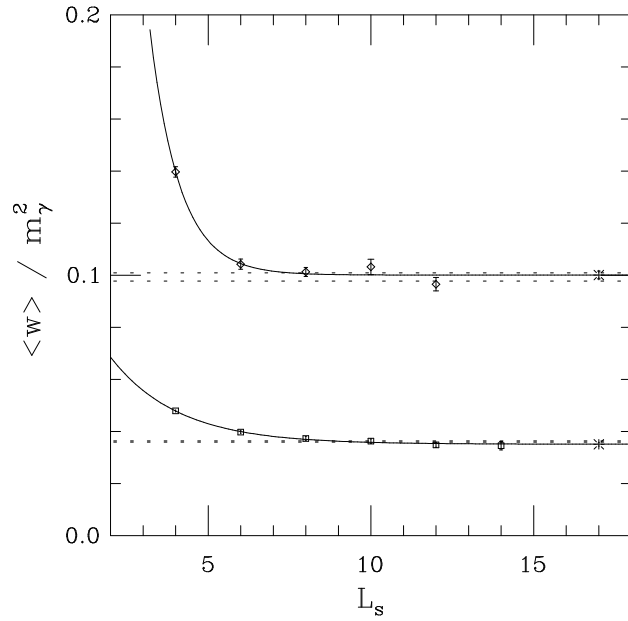


Figure 18. $\langle w \rangle / m_\gamma^2$ vs. L_s . The parameters are as in figure 17.